H20-rich mantle melting near the slab–wedge interface

Citation: Contributions to Mineralogy and Petrology. 2019 Sep 17;174(10):80

As Published: https://doi.org/10.1007/s00410-019-1615-1

Publisher: Springer Berlin Heidelberg

Persistent URL: https://hdl.handle.net/1721.1/131419

Version: Author's final manuscript: final author's manuscript post peer review, without publisher's formatting or copy editing

H_2O-rich mantle melting near the slab–wedge interface

Cite this article as: Timothy L. Grove and Christy B. Till, H_2O-rich mantle melting near the slab–wedge interface, Contributions to Mineralogy and Petrology https://doi.org/10.1007/s00410-019-1615-1

H_2O-rich mantle melting near the slab – wedge interface

Timothy L. Grove[1] and Christy B. Till[2]

[1]Department of Earth, Atmospheric and Planetary Sciences,
Massachusetts Institute of Technology, Cambridge, MA 02139

[2]School of Earth and Space Exploration
Arizona State University, 781 E Terrace Mall
Tempe, AZ 85287

Abstract

In order to investigate the first melts of the mantle wedge in subduction zones and their relationship to primitive magmas erupted at arcs, the compositions of low degree melts of hydrous garnet lherzolite have been experimentally-determined at 3.2 GPa over the temperature range of 925 to 1150°C. Two starting compositions with variable H_2O contents were studied; a subduction-enriched peridotite containing 0.61 % Na_2O, 0.16 K_2O % (wt. %) with 4.2 wt. % H_2O added (Mitchell and Grove, 2015) and an undepleted mantle peridotite (Hart and Zindler, 1986) with 14.5 % H_2O added (Till et al., 2012). Saturating phases include olivine, orthopyroxene, clinopyroxene, garnet and rutile. Melting extent is tracked from near solidus (~ 5 wt. %) to 25 wt. %, which is close to or beyond the point where clinopyroxene and garnet are exhausted. The beginning of melting is a peritectic reaction where 0.54 orthopyroxene + 0.17 clinopyroxene + 0.13 garnet react to produce 1.0 liquid + 0.88 olivine. The melt production rate near the solidus is 0.1 wt. % $^oC^{-1}$ and increases to 0.3 wt. % $^oC^{-1}$ over the experimentally studied interval. These values are significantly lower than that observed for anhydrous lherzolite (~1 wt. % $^oC^{-1}$). When melting through this reaction is calculated for a metasomatized lherzolite source, the rare earth element characteristics of the melt are similar to melts of an eclogite, as well as those observed in many subduction zone magmas. Moreover, since rutile is stable up to ~8 wt. % melting, the first melts of a hydrous lherzolite source could also show strong high field strength element depletions as is observed in many subduction zone lavas. The silicate melts measured at the lowest temperatures and melting extents (< 10 wt. %) are high silica andesites (56-60 wt. % SiO_2) and contain very low Ca/Al and high alkalis. These deep low degree andesitic melts, if added to experimentally-produced hydrous liquids from melting (20 – 25 wt. %) of harzburgite residues at shallow pressures (1.0 to 1.2 GPa, Mitchell and Grove, 2015), can match the compositional characteristics of primitive natural basaltic andesite and magnesian andesite lavas found globally in arcs.

In addition to a silicate melt phase, there is a small amount of silicate dissolved in the H_2O supercritical fluid that coexists with the silicate liquid and solids in our experiments. The composition of this fluid is in equilibrium with the Mg-rich minerals and it is granitic. The results presented here are used to develop a model for producing hydrous arc magmas. We hypothesize that mantle wedge melting produced by the flux of hydrous fluid from the slab occurs over a range of depths that begins at the base of the mantle wedge and ends at shallow mantle depths. These melts ascend and remain isolated until they mix in the shallow, hottest part of the mantle wedge. In this melting scenario, the metasomatic "slab melt" contributions to arc magmas is small (~ 5 wt. %), but its effect on the alkali, REE and incompatible trace element budget of the derivative magmas is large, and able to reproduce the trace elemental characteristics of the primitive andesites. Higher proportions of slab or sediment melt do not resemble primitive high magnesian arc andesites and basaltic andesites.

Introduction

It is generally accepted that partial melting of peridotite in subduction zones is initiated by an influx of volatiles from the subducted ocean lithosphere (e.g., Gill, 1981; Tatsumi et al., 1986; Davies and Stevenson, 1992). However, the specifics of the mantle melting process, as well as the composition of the hydrous partial melts generated, have been the subject of experimental investigations and scientific debate for more than 45 years. Much of our understanding about these melts comes from the early experimental work of Kushiro and co-workers, that focused on using simplified compositional systems, such as Mg_2SiO_4-SiO_2-H_2O (Kushiro et al., 1968; Kushiro 1968, 1972). This pioneering work suggested hydrous peridotite melting produces SiO_2-rich melt; consistent with the hypothesis that andesite magmas erupted at arc volcanoes are the descendants of partial melts of hydrous mantle peridotite (Poldervaart, 1955; Kushiro, 1972). Later experimental studies on natural peridotite compositions indeed produced hydrous glasses high in SiO_2 and low in FeO and MgO (Kushiro, 1972; Mysen and Boettcher, 1975a,b; Nehru and Wyllie, 1975) but raised questions regarding the modification of melt composition via growth of amphibole and pyroxene upon quench (e.g., Green, 1973; 1976). Careful experimental studies by Gaetani and Grove (1998, 2003) at 1100-1345°C and 1.2-2 GPa demonstrated that the addition of 3-6 wt.% H_2O in spinel lherzolite melts increases SiO_2 by ~1 wt.% and decreases FeO + MgO by ~2 wt.% relative to analogous anhydrous peridotite melts because of the lower temperature of melting in the presence of H_2O. These results also supported the interpretation that parental arc magmas with high pre-eruptive H_2O contents form when fluid-

saturated peridotite partial melts percolate upward in the mantle wedge and maintain equilibrium with the hotter overlying peridotite (i.e., reactive porous flow).

Within the last decade, new petrologic evidence has arisen that resolves the long-standing discrepancy in the solidus temperature of the H_2O-saturated mantle and demonstrates that mantle peridotite melts at extremely low temperatures when in the presence of excess water. The long-duration high-pressure mantle melting experiments by Grove et al. (2006) and Till et al. (2012) indicate that the H_2O-saturated peridotite solidus is located between 800° and 820°C at 3-6 GPa. Likewise, studies of a peridotite massif exposed in the Japanese Sanbagawa belt (Hattori et al., 2009; Till et al., 2009) find evidence for hydrous melting processes at ~800°C and ~3 GPa in a paleo-mantle wedge. The work presented here focuses on the analysis of the compositions of these near solidus hydrous lherzolite melts. We have performed a series of experiments at 3.2 GPa using a metasomatized lherzolite bulk composition containing 4.2 wt. % H_2O, as well as present new analyses of the silicate melt and quenched supercritical fluid from the 3.2 GPa experiments of Till et al. (2012) that used an undepleted lherzolite bulk composition containing 14.5 wt. % H_2O. These experiments and analyses shed new light on the composition of hydrous partial melts and the specifics of hydrous melting behavior deep in the mantle wedge at subduction zones. We will also compare these melt compositions to those produced in the work of Green et al. (2010, 2014), the classic study of Mysen and Boettcher (1975a,b), other H_2O-bering lherzolite melts produced at similar pressure – temperature conditions (Tenner et al., 2012; Mallik et al., 2015; Gaetani and Grove, 1998) and anhydrous lherzolite melts produced at similar pressures (Grove et al., 2013; Brown et al., 2019).

Experimental and Analytical Methods

Starting materials

Two different starting materials were used in this study. The first is the primitive upper mantle composition of Hart and Zindler (1986) (H&Z+H_2O) that was synthesized by combining high-purity synthetic oxides or metasilicates in the appropriate proportions with Brucite, $Mg(OH)_2$, added to the synthetic oxide mixture instead of MgO, which provided the starting composition with ~14.5 wt.% H_2O. This is the composition used by Grove et al. (2006) and Till et al. (2012).

The second composition is the synthetic oxide Mix D of Mitchell and Grove (2015) (hereafter referred to as wet H&Z+SM), which is a combination of 29% of the first hydrous starting mix

(H&Z+H_2O) used by Grove et al. (2006) and Till et al. (2012), and 71% an anhydrous version of the Hart & Zindler (1986) primitive mantle composition with a metasomatic slab component added (dry H&Z+SM) (Table 1). The dry H&Z+SM starting mix includes additional alkalis (~ 5 wt. % of the total) to simulate the addition of these components from a melt of a subducted slab based on the Grove et al. (2002) estimate of a slab component.

Piston cylinder experiments

The details of the experiments that used the H&Z+H_2O composition are reported in full in Till et al. (2012). These experiments were reanalyzed to obtain the composition of the melt phase in this study. The melting experiments on H&Z+SM were carried out at 3.2 GPa over the temperature range from 925 – 1150^{o}C using a 0.5" end-loaded solid medium piston cylinder (Boyd and England, 1960) in the MIT Experimental Petrology Laboratory. For each experiment, starting material was packed into an Au capsule, which was then triple crimped and welded and placed inside an Al_2O_3 ring. The capsule and Al_2O_3 ring were sandwiched between MgO spacers in the midpoint of a cylindrical graphite furnace. Surrounding the graphite furnace was a sintered, cylindrical $BaCO_3$ pressure cell.

The experiments were conducted using the hot piston-in technique (Johannes et al., 1971). At the beginning of each run, the assembly was pressurized at room temperature to 1.0 GPa. Temperature was raised at a rate of 100˚C/ minute until 865˚C, where it was held for six minutes. Then, pressure was raised to the final pressure, and temperature was increased at 50˚C/minute to the final temperature of the run. Experiments were held at their final run conditions for 48 to 292 hours. The experiment was terminated by turning off the power.

Pressure was previously calibrated using the breakdown of Ca-tschermak pyroxene to anorthite + gehlenite + corundum (1,350 ˚C, 1.3 GPa) and using the spinel (sp) to garnet transition in the CMAS peridotite analog system (1,500 ˚C, 2.5 GPa) (Hays, 1966; Longhi, 2005). This calibration showed that pressure was accurate to ±0.05 GPa, and that no pressure correction was necessary.

Temperature was monitored and controlled using $W_{97}Re_3/W_{75}Re_{25}$ thermocouples without correction for the effect of pressure on thermocouple emf. The vertical thermal gradient across the charge has been determined by direct measurement of offset thermocouples as well as temperature mapping using the reaction kinetics of $MgO + Al_2O_3 = MgAl_2O_4$ (Watson et al. 2002; Médard and Grove, 2008). Results from these methods indicated a vertical temperature difference of ~10˚C across the capsule (hot end on top) in addition to a ~20˚C difference between

the location of the hotspot in the graphite furnace and the location of the thermocouple 1.5 mm above the capsule. Temperature corrections for this ~20˚C difference were applied.

Electron microprobe analysis

The major element concentrations of all experimental products were analyzed by wavelength dispersive spectrometry on the 5-spectrometer JEOL 8200 electron microprobe (EMP) at the Massachusetts Institute of Technology. All analyses of minerals were conducted with a 15 kV accelerating voltage, a 10 nA beam current and a 1 μm spot size. Quench-modified melt analyses were conducted with a range of beam currents (3 to 10 nA), and spot sizes (1-10 μm) and measurement times (5-40 sec), depending on the size and fragility of the quench product. Online data reduction utilized the CITZAF correction package (Armstrong, 1995) and the atomic number correction, the absorption coefficients, and the fluorescence correction available in CITZAF.

Experimental Results

Mineral and Melt Textures

The temperature conditions and mineral phase assemblages of the experiments reported in this paper are shown in Figure 1. Experimental durations, phase proportions are reported in Table 2 and the compositions of phases are reported in Tables 3 and 4. For the wet H&Z+SM composition (4.2 wt. % H_2O bulk) all of the experiments contained olivine (oliv) + orthopyroxene (opx) + clinopyroxene (cpx) + garnet + liquid. Below 950˚C rutile becomes a saturating phase. Experiments on the H&Z+H_2O composition (14.5 wt. % H_2O bulk) from Till et al. (2012) were chosen that contained analyzable patches of glass. In these, experiments above 1100˚C contain oliv + opx + spinel + liquid. The three lower temperature experiments analyzed here contained cpx + garnet in addition to oliv + opx + melt.

During the experimental studies of Grove et al. (2006) and Till et al. (2012), the experimental charges were cut in half, impregnated with epoxy, and then polished on diamond impregnated mylar film using polishing oil. This sample preparation technique preserves the quench-modified melt phase that is present in between the mineral grains in the experiment. Occasionally larger pools of quench-modified glass were encountered and these are shown in Figure 2a, b. Even in the lower temperature experiments (e.g., Fig. 2c, 1000˚C, 9 % melt), the quench-modified melt pockets could be hundreds of microns in size. In the higher temperature

experiments, the melt phase would collect in mm-sized layers across the top of the charge (Fig. 2a, 1150°C, 27.5 % melt). These quench-modified melt pockets were always near the top, higher temperature end of the capsule. Melt would also pool in horizontal Au septa that formed when the capsule was flattened after welding (e.g., Fig. 2c). As our sample preparation techniques evolved, we developed several techniques that allowed us to maximize the possibility of finding melt pools. One was to slice the charge into four pieces with a diamond wire saw, visually inspect each side of the slice and mount up surfaces that looked promising for revealing a melt segregation pool. Another was to polish very carefully on the diamond lapping paper to keep the quench-modified melt from plucking out.

In the higher temperature experiment that contained higher melt fractions (≥1075^{o}C), the melt quenched to a mat of crystals + glass (Fig. 3 a, Fig. 2a, b). In the lower temperature experiments (≤1050^{o}C), the quench-modified melt occurred as microns-thick sheets that formed in voids created by the decompression during quenching. These sheets were preserved when the sample was impregnated with epoxy (Fig. 3b,d) or preserved as partly plucked out unpolished regions (Fig. 3c) where multiple layers of thin sheets could be observed curving over and around underlying crystals. Also present were isolated spheres of melt (Fig. 3b,d) that were distinctly different in composition. As shown in Figure 4, the two melts were easily distinguished by shape and occurrence in the quenched sample. The Backscattered Electron Image (Fig. 4a) shows the compositional contrast between the crystals and the melt phases impregnated in epoxy and present in plucked out regions and the Secondary Electron Image (Fig.4b) shows the spatial relationships among the crystals and melt phases. The thin melt sheets along the lower edge of Fig. 4b were preserved during impregnation by epoxy. In the upper right of Fig. 4b to the right of the olivine crystal (oliv), plucking of crystals during polishing reveals the 3-D complexity of the thin melt sheets. Also present are vesicles presumed to have been filled with H_2O-rich supercritical fluid during the experiment. Upon quenching, the fluid is thought to have precipitated the spheres in the vesicles. In Fig. 4a, a vesicle near the center of the image is surrounded by the melt phase, which can be seen as folded over sheets to the right of the vesicle. Below and to the right of the exposed sphere-lined vesicle are two irregular holes (Fig. 4b) that expose vesicles lower in the charge that expanded upon quenching and became surrounded with the thin melt sheets that wrap around them and then were preserved in the epoxy. The chemical composition of the spheres and melt sheets, further discussed below, are also diagnostic and always correlated with the morphology (Table 3, 4).

Textures of the minerals in the experimental run products in this study were very similar to those produced in our previous studies (Grove et al., 2006; Till et al., 2012). Olivine crystals

are euhedral to subhedral (25 – 100 microns) and orthopyroxene and clinopyroxene are equant to subhedral to elongate and varied in size depending on temperature from ~20 to 40 microns. Garnet was always the largest mineral in the charge (100 to 200 microns) and it poikilitically encloses the other minerals. Garnet and clinopyroxene are commonly present on the bottom (colder end) of the capsule. Rutile was present as isolated 20 – 50 microns crystals. See Supplementary Figure 1 for images of all H&Z+SM experiments discussed in this paper.

Mineral and melt compositions approach to equilibrium and oxygen fugacity

For the solid mineral phases, 10 to 20 analyses of each phase were made throughout the charge and the low standard deviations of these analyses (Table 3) demonstrates that the minerals were unzoned and compositionally homogenous in each experiment. The quench-modified melt was analyzed using two different approaches. For the higher temperature experiments (≥1075^{o}C: D287, D284 and D279), the large quench-modified melt regions consisted of glass and quench-grown minerals inferred to be amphibole and clinopyroxene, and were analyzed as a grid of 100's of points set up at > 10-micron intervals. This grid of points was then averaged and was assumed to be representative of the composition of the melt phase. In the lower temperature experiments containing the thin melt sheets and spheres (≤1050^{o}C: D255, D250, D252, D260, and D266), electron microprobe analysis points were set up individually on the quench-modified melt and analyzed using a 2 – 3 micron spot. These thin melt sheets were challenging to analyze. The microprobe beam often fell on quench- grown minerals. Also, the micron-thick sheet was often draped over larger equilibrium minerals that were just under the quench melt sheet and these minerals were within the excitation volume of the electron beam, resulting in a mixed analysis. In contrast, the granitic melt spheres were easier to analyze. They did not contain quench crystals, larger spheres could be found an analyzed, and the analyses were more homogeneous.

Collectively, the "melt" analyses consist of a mixture of quench-modified melt, quench-grown crystals, and melt with mixed with underlying crystals. As such many melt analyses have high MgO and high Mg# analyses contaminated by minerals. The data was filtered to remove these over-represented analyses (> 24 wt. % MgO and attendant high Mg# > 84) and < 42 % SiO_2. All of the low-temperature quench-modified melt and quench-mineral analyses were arranged in order of decreasing MgO content and Mg#. The analyses with the highest % MgO and attendant highest Mg# (Mg# > 84) were deleted in order of decreasing values until the overall average of quench-modified melt and high MgO quench crystals was equivalent to the Mg# values of the super-critical-derived fluid spheres analyzed in the same experiment. The justification for doing this is that the two phases, H_2O-rich silicate melt and the dominantly H_2O silicate-bearing

supercritical fluid are both in equilibrium with the same silicate mineral assemblage. The errors on the melt phases are presented in Tables 3 and 4, as the standard deviation of the mean. For all other phases the raw sample standard deviation is reported..

The long experimental durations of these experiments were essential for the achievement of equilibrium, which was evidenced by the following: 1) within mineral grains, there was no chemical zoning and the compositions were constant, 2) the compositions of mineral phases across the entire charge were constant with and textures were consistent with equilibrium growth, and 3) the changes in mineral and melt compositions with changing temperature were systematic and predictable. This third criterion is evident in the partitioning of Fe and Mg among the coexisting olivine, orthopyroxene, clinopyroxene, garnet and melt phase similar to that demonstrated by Till et al. (2012). The olivine/silicate melt Fe/Mg exchange coefficient ($K_D^{Mg\text{-}Fe}{}_{Oliv\text{-}Liq}$) can provide evidence of the attainment of equilibrium between mineral phases and coexisting melt. In the two highest temperature experiments, the $K_D^{Mg\text{-}Fe}{}_{Oliv\text{-}Liq}$ was 0.330 to 0.345. In the lower temperature experiments, the $K_D^{Mg\text{-}Fe}{}_{Oliv\text{-}Liq}$ ranged between 0.345 and 0.388 with an average value of 0.360 +/- 0.015. Partitioning of Fe and Mg between the coexisting solids was also regular and well behaved. The $K_D^{Mg\text{-}Fe}{}_{Oliv\text{-}Opx}$, $K_D^{Mg\text{-}Fe}{}_{Oliv\text{-}Cpx}$ and $K_D^{Mg\text{-}Fe}{}_{Oliv\text{-}Garnet}$ were 1.09 ± 0.02, 1.26 ± 0.04, and 0.443 ± 0.04, respectively (reported as one standard deviation). The value of $K_D^{Mg\text{-}Fe}{}_{Oliv\text{-}Liq}$ originally measured by Roeder and Emslie (1970) was found to be constant at a value of 0.30. As more experimental data on olivine/melt partitioning has accumulated, the value for $K_D^{Mg\text{-}Fe}{}_{Oliv\text{-}Liq}$ in experiments has been found to be variable and to range from between ~0.17-0.45 (Toplis, 2005). Pressure, temperature, olivine composition, melt composition, and water content are potential sources of variation in $K_D^{Mg\text{-}Fe}{}_{Oliv\text{-}Liq}$ (e.g., Mysen 1975, Ulmer, 1989; Kushiro and Walter, 1998; Toplis, 2005). Toplis (2005) developed a model that predicts the effects of these variables on the $K_D^{Mg\text{-}Fe}{}_{Oliv\text{-}Liq}$. This expression (Equation 10 in Toplis, 2005) was used to predict the $K_D^{Mg\text{-}Fe}{}_{Oliv\text{-}Liq}$ for these experiments. Using an estimate of H_2O content (~ 30 wt. %), the predicted value of $K_D^{Mg\text{-}Fe}{}_{Oliv\text{-}Liq}$ is 0.315. This is lower than the values measured here, but the experiments reported here fall well outside the calibration range of the Toplis (2005) model in terms of temperature, pressure, and water content. Experiments by Gaetani and Grove (1998) and Ulmer (1989) suggest that H_2O likely increases the value of the $K_D^{Mg\text{-}Fe}{}_{Oliv\text{-}Liq}$ relative to anhydrous melting experiments (Toplis, 2005), so the mismatch between the Toplis model and the measured values reported here may result from these differences.

Iron loss/gain in our experiments was less than +/- 5 % for all of the experiments reported here (Table 2), indicating little to no interaction between the Au capsule and the silicate charge. Oxygen fugacity was not specifically measured in these experiments, but in similar run

assemblies used in Grove et al. (2006) and Mandler and Grove (2016), it was estimated from mineral equilbria to be between QFM +1 and QFM-2.

Discussion

Compositions of near solidus melts of hydrous lherzolite

In Figure 5 the compositions of analyzed melts from the H&Z+SM and H&Z+H_2O experiments are plotted vs. temperature along with those from Mysen and Boettcher (1975a,b) (M&B'75). The M&B'75 experiments were carried out on a lherzolite composition containing 5 wt. % H_2O and are therefore the most analogous experiments to compare to our results. The M&B'75 liquids are from experiments conducted at 1.5 GPa, opposed to our 3.2 GPa conditions. Both the H&Z+H_2O and H&Z+SM melt compositions show similar variations with changing temperature. Both the H&Z+H_2O and the H&Z+SM melts start out with high SiO_2 (58 – 60 wt. %, Fig. 5a) that drops with increasing temperature to ~ 50 – 52 wt. % SiO_2. In contrast the M&B'75 melts are all high SiO_2 (55 – 65 wt. % SiO_2). The most striking characteristic of the H&Z+H_2O and the H&Z+SM melts is the variation in CaO with increasing temperature. Over the temperature range of 950 – 1050^{o}C, the CaO content of the melts is 1 – 2 wt.% CaO (Fig. 5b), which rises rapidly as temperature increases. The changes in CaO with melting results from changes in the proportion of clinopyroxene and garnet consumed during melting. At low temperatures, clinopyroxene is only a small fraction of the melting assemblage. Above 1075 ^{o}C, the melting reaction changes and clinopyroxene consumption increases rapidly (see *Hydrous lherzolite melting reactions and melt production*). In contrast, CaO remains at 10 wt.% across all temperatures in the M&B'75 experiments. Over the comparable temperature interval (950 – 1050 ^{o}C), the H&Z+H_2O and H&Z+SM melts have Al_2O_3 contents of ~ 15 wt. % (Fig. 5c), while the M&B'75 experiments are characterized by high Al_2O_3 contents of ~ 20 - 25 wt. %, which then drop to ~15 wt. % with increasing temperature. The differences between the M&B'75 1.5 GPa melt compositions and the 3.2 GPa melts are a result of the effects of H_2O and pressure on melt composition and on differences in the residual phases and differences in the melting reaction. The phase assemblage in the M&B'75 experiments is olivine, orthopyroxene, clinopyroxene, and amphibole, and the melting reaction consumes amphibole and clinopyroxene in greater proportions early on, resulting in higher CaO in the melt. As temperature increases the MgO and FeO contents of melt in the H&Z+H_2O and H&Z+SM experiments increase from low values of 7 wt. % MgO and 5 wt. % FeO to values of 16 % and 8 % respectively (Fig.5d, 4e). In contrast the

lower pressure experiments of M&B'75 remain low in both MgO (2-5 wt. %) and FeO (~1 – 2 wt. %). The Na_2O content of melts from the H&Z+H_2O experiments that contained 14.5 wt.% H_2O are significantly lower (~1 wt. %Na_2O) than the H&Z+SM experiments that contained 4 wt. % H_2O (~2-4 wt. % Na_2O). This is because the significant solubility of Na_2O in the fluid phase as noted by Green et al. (2010) and Mandler and Grove (2016). It is also probable that Na_2O was lost during the electron microprobe analysis by Na migration in the glass.

Spheres found in the voids between quenched melt wisps in experiments at 1075°C and below (Fig. 4) produce compositions with >70 wt.% SiO_2 at <2 wt.% MgO (Table 3). As discussed in the prior section (*Mineral and melt textures*) we interpret the spheres as quench products that exsolved from the supercritical vapor phase that was present with the melt phase, similar to the interpretation of White and Wyllie (1992). The absence of these spheres in the three highest temperature H&Z+SM experiments with the lower H_2O content (4 wt. % H_2O bulk) is most likely due to the change from vapor-saturated to vapor-undersaturated melting at these conditions. In contrast, granitic spheres are present in experiments on the H&Z+H2O composition (14.5 wt. % H_2O bulk) at the highest temperatures run by Till et al. (2012, see their Fig.6).

The melting experiments on hydrous lherzolite compositions are also shown plotted in pseudoternary subprojections in the pseudoquaternary system Olivine – Clinopyroxene – Garnet – Quartz (Qtz) in Figure 6 (the recalculation scheme is presented in Supplementary Table1). In the Olivine – Garnet – Quartz and Olivine – Clinopyroxene – Quartz subprojections, the low temperature H&Z+H_2O and the H&Z+SM melts start out with at Quartz-normative compositions that move toward the Garnet and Clinopyroxene corner of each pseudoternary and into silica undersaturated space (i.e., negative Quartz values) as melting proceeds. The M&B'75 melts do not plot in this pseudoquaternary space, but plot to the right of the Garnet – Clinopyroxene – Quartz face at high negative values of the Olivine component. This is a reflection of their high normative plagioclase and SiO_2 values. The granitic spheres plot close to the Quartz apex.

Comparisons with previous experimental studies on hydrous lherzolite melting

The oxide vs. SiO_2 variation diagrams in Figure 7 compare the experimental hydrous melts of garnet lherzolite with a suite of other relevant prior experimental observations. Tenner et al. (2012) carried out experiments at 3.5 GPa and produced a liquid saturated with olivine, orthopyroxene, clinopyroxene and garnet and three liquids containing olivine, orthopyroxene, and garnet between 1275 and 1375°C. The H_2O content of these liquids varies between 6 and 11 wt. % H_2O. In contrast to our lower temperature melts, the Tenner et al. (2012) melts are high in

MgO (18 – 23 wt. %), low in SiO_2 (42- 48 wt. %) and very low in Na_2O and K_2O (<< 1 wt. %). These liquids are ultramafic and silica-undersaturated. When projected into pseudoquaternary subprojections (Fig. 8), they plot at negative Quartz values. At these higher pressures of 3.5 GPa melting of hydrated lherzolite rapidly exhausts clinopyroxene at low melt fractions (F = 0.20-0.23), in a manner similar to our 3.2 GPa experiments.

At similar pressures to our experiments, Mallik et al. (2015) report liquids saturated with olivine, orthopyroxene, clinopyroxene, garnet and phlogopite between 1150 and 1300°C at 3 GPa. The Mallik et al. (2015) experiments were performed using a starting composition that was a mixture of 25 % rhyolite and 75 % peridotite which significantly increases the bulk K_2O content and leads to very high K_2O, and strongly silica-undersaturated melts (Fig. 7f). When the Mallik et al.(2015) experimental melts are projected into pseudoquaternary subprojections (Fig. 8), they also plot at negative Qtz values. The H_2O content of these liquids varied between 6 and 8 wt. % H_2O. In contrast to our lower temperature melts, the Mallik et al. (2015) melts contain 13 – 14 wt. % MgO, with 49 – 50 wt. % SiO_2 and very high Na_2O and K_2O (2.5 % Na_2O and > 7 % K_2O). The amount of melt present is these experiments (F = 0.20-0.25) is consistent with their high temperatures.

As illustrated in Figure 1, Green et al. (2010; 2014) put the hydrous lherzolite solidus at 1075 – 1100°C (Fig. 1) at 3 GPa. The Green et al. (2010, 2014) experiments also used H&Z primitive mantle as a starting composition. In both our experiments and those of M&B'75, analyzable melt pools are present at temperatures 200°C lower than the Green et al. (2010; 2014) solidus. The two melt compositions reported by Green et al. (2014) at 2.5 GPa, 1050°C with 1.45 wt.% H_2O stand out from other hydrous garnet-saturated melts in having much higher Na_2O and lower FeO (Fig. 5).

Five hydrous garnet lherzolite + basalt melting experiments at 1.6 and 2 GPa from Gaetani and Grove (1998) are transitional to silica-undersaturated basaltic melts with higher SiO_2 (47-48 wt. %) and lower MgO (12 – 14 wt. %) (Fig. 7, 8). These liquids contained 6 – 11 wt. % H_2O. As discussed by Gaetani and Grove (1998) these melt compositions contain higher SiO_2/(FeO + MgO) in comparison to anhydrous lherzolite melts produced at similar pressures.

Also shown for comparison in Figures 7 and 8 are 3.2 GPa anhydrous batch (1 to 15 wt %) melts of the H&Z bulk composition calculated using the garnet lherzolite melting model of Grove et al. (2013) as updated by Brown et al. (2019) (Supplementary Table 2). These melts form at considerably higher temperatures (1 wt. % melt @1549°C) than the H_2O-undersaturated garnet lherzolite melts and the experiments presented in this paper (e.g., 5 wt. % melt in the wet H&Z+SM experiments at 950°C). In Figure 7, the low degree anhydrous melts plot at the lowest

SiO_2 values and SiO_2 increases as melt % increases. In Figure 8, the 1 wt. % melt is the most silica-undersaturated and continued melting increases the Quartz component, followed by increasing Garnet and Clinopyroxene components. Interestingly, these anhydrous low-degree melts resemble the higher degree H_2O undersaturated melts. They are low in silica, high in FeO and MgO, and have similar CaO and Al_2O_3 abundances to the hydrous higher degree melts.

Comparison to Natural Primitive Basaltic Andesites & Magnesian Andesites

Also shown in Figures 7 and 8 are the compositions of primitive arc basaltic andesites and magnesian andesites. The compositions of hydrous experimentally produced mantle melts tend to surround these primitive natural lavas with few or none explicitly matching their compositional characteristics. Most of the basaltic experimental melts plot at lower silica relative to the natural arc andesitic lavas (Fig. 7) and in silica-undersaturated composition space in the pseudoternary diagrams (Fig. 8). Interestingly, the experimental data sets of H_2O-saturated lherzolite melting from M&B'75 at 1.5 GPa and the 3.2 GPa wet H&Z+SM and H&Z+H_2O experimental data both span the same range of SiO_2 values as the natural lavas. In SiO_2 vs. Al_2O_3, FeO and MgO, the wet H&Z+SM and H&Z+H_2O melts overlap the range of natural lavas and trend toward higher MgO while the M&B'75 liquids have lower MgO. In CaO vs. SiO_2, the wet H&Z+SM and H&Z+H_2O melts have very low CaO at low melt fractions and CaO increases as more clinopyroxene is melted out of the solid residual mineral assemblage. The M&B'75 liquids plot at higher values of ~10 wt. % CaO. In Al_2O_3 vs. SiO_2 the 3.2 GPa melts overlap in Al_2O_3 with the natural lavas and the M&B'75 liquids have very high Al_2O_3 of 20 – 25 wt. %. Only in the FeO vs. SiO_2 plot do the compositions of the 3.2 GPa garnet-saturated hydrous melts overlap with the natural primitive andesites and the M&B75 melts are very low at 2 wt. % FeO. The differences in the natural primitive lavas, the H&Z+SM and H&Z+H_2O hydrous melts, and the 1.5 GPa M&B'75 liquids also show up in the pseudoquaternary space (Fig. 8). As a consequence of the very high Al_2O_3, the M&B'75 liquids plot far away from the natural primitive liquids.

Mitchell and Grove (2015) find that they can match many of the compositional characteristics (e.g., MgO, Al_2O_3, SiO_2, FeO, Na_2O, [Fig. 9a-c, 9e]) of the primitive natural basaltic andesite and magnesian andesite lavas with experimentally produced hydrous liquids containing 4 – 6 wt. % H_2O from melting (20 – 25 wt. %) of harzburgite residues at pressures of 1.0 to 1.2 GPa. The compositions of a subset of the primitive basaltic andesite and magnesian andesite lavas shown in Figures 7 and 8 are shown again in Figure 9 along with the experimentally-produced hydrous liquids from melting of harzburgite residues at pressures of 1.0 to 1.2 GPa from Mitchell and Grove (2015) and the low-temperature, low-degree (5 to 10 wt. %)

hydrous 3.2 GPa lherzolite melts reported in this paper. The natural primitive lavas are subdivided according to subduction zone with lavas from the Cascades, Kamchatka and the Setouchi belt highlighted. The natural lavas all are consistent with experimentally-determined multiple saturation with olivine + orthopyroxene residual mantle assemblages at these shallow pressures (Mitchell and Grove, 2015; Grove et al., 2012; Gaetani and Grove, 2003). However, they could not match the natural lavas in terms of abundances of CaO and K_2O (Fig. 9d, f). The abundances of CaO, in particular, were variable from arc to arc and lower than the abundances found in the low pressure, hydrous high % harzburgite liquids. In addition, the K_2O abundances in these natural primitive lavas are higher than found in the low pressure, hydrous high % harzburgite liquids. A mass balance on CaO using the high degree harzburgite melts and the hydrous, low degree 3.2 GPa melts shows that a combination of ~45 wt. % of a 3.2 GPa low-degree melt component and 55 wt. % harzburgite melt could match the CaO abundances in the Setouchi primitive lavas, and 40:60 wt. % for Kamchatka. To mass balance CaO in the most primitive basaltic andesites at Mt. Shasta requires a contribution of ~12 wt. % of the hydrous 3.2 GPa melt with the remainder harzburgitic, but other primitive magnesian andesite lavas at Mt. Shasta require higher amounts (30 – 45 wt. %).

Another compositional characteristic of the natural primitive basaltic andesite and magnesian andesite is the strong garnet signature in their rare earth element abundance patterns (Grove et al., 2002). We propose in the next section that the elemental characteristic of the melts produced during deep, hydrous, low-degree melting of a metasomatized lherzolite near the slab – wedge interface contribute this component.

Hydrous lherzolite melting reactions and melt production at 3.2 GPa

The changes in mineral and melt proportions obtained from mass balance of the 4 wt. % H_2O H&Z+SM composition are tabulated in Table 2. At the lowest temperatures where melt could be analyzed (950°C), olivine is the most abundant mineral phase and orthopyroxene, high-Ca clinopyroxene and garnet are present at about 10 – 12 weight % each. Over the temperature interval from 950° to 1050°C, the melting reaction and melting rate have been determined using the method of Kinzler (1997, see her Table 4) to determine the stoichiometric coefficients of the melt reaction. Experiments D252 and D260 yield the melting reaction:

0.54 opx + 0.17 cpx + 0.13 garnet = 1.0 melt + 0.88 oliv

The melting reaction is peritectic and orthopyroxene, high-Ca clinopyroxene and garnet melt incongruently to olivine and liquid. The calculated melting rate is 0.1 % melt/^{o}C. At the high temperature end of the experiments on the wet H&Z+SM composition (1075 – 1125 ^{o}C), the melting rate increases significantly and the melting reaction changes. Experiments D287 and D279 yield the melting reaction:

0.09 oliv + 0.49 cpx + 0.64 garnet = 1.0 melt + 0.13 opx

The calculated melting rate rises to 0.27 % melt/^{o}C. This melting reaction is similar to the one found for dry lherzolite melting in the garnet stability field (Walter, 1998; Grove et al, 2013) in that they both have orthopyroxene on the melt side of the reaction. The change in the melt reaction is caused by the melt changing from silica-saturated at low temperatures, to silica-undersaturated at high temperatures. At the low temperatures of hydrous melting, the melt composition is very low in CaO (> 1 wt. %) and this is because the low temperature melting reaction is mostly consuming orthopyroxene and only small sub-equal amounts of clinopyroxene and garnet. When the melt changes to silica-undersaturated compositions and the melting rate increases, CaO increases rapidly as clinopyroxene and garnet now dominate the melting reaction. Figure 10 illustrates these two contrasting low- and high-temperature melting reactions, with the switch in the peritectic mineral occurring because of the change in melt composition. Olivine, orthopyroxene, clinopyroxene and garnet are nearly pure end member phases, and so they plot at the apices of the pseudoquaternary system. The movement of the melt creates the switch from olivine to orthopyroxene as the peritectic mineral.

Gaetani and Grove (1998) also calculate $(dF/dT)_P$ = ~0.05%/°C at 2% partial melt for a peridotite with 0.15 wt.% H_2O at 1.5 GPa and find the productivity increases continuously to 0.80%/°C at 20% partial melt. Studies of anhydrous peridotite melting determine an average melt productivity of ~0.30%/°C for ~20-40% partial melt at both 1 and 3 GPa (Baker and Stolper, 1994; Walter, 1998; Falloon and Danyushevsky, 2000) and values of 0.8-1.27%/°C for fertile peridotite at ~2 GPa (Kinzler, 1997). These observations indicate the concentration of dissolved H_2O in the melt exerts an important control on melt productivity. The extremely low melt production rate determined here for the H_2O-saturated 20-30% melts of Till et al. (2012) and the H_2O-saturated 2% partial melts of Gaetani and Grove (1998), suggest that a melt production rate of ~0.05-0.13%/°C may be a minimum bound on peridotite melting rates common to H_2O-saturated melts. These low rates of melt production suggest a significantly longer melting

column is required to produce the same amount of partial melt generated in anhydrous partial melting environments.

Trace element characteristics of low-degree mantle melts

These experimental results on the compositions low degree melts and the melting reactions that take place near the base of the mantle through the addition of an H_2O-bearing metasomatic component allow us to test models for interpreting the trace element characteristics of hydrous melts. To infer the trace element composition of a melt of metasomatized garnet lherzolite, we combine the rare earth and incompatible trace element abundances of 90% primitive lherzolite (Hart and Zindler, 1986 with trace element abundances from Hoffman ,1988), with 10% "fluid-rich slab component," as estimated by removing a harzburgitic mantle melt from primitive Mt. Shasta basaltic andesites and assigning the remaining elements to the H_2O component in the lava (see Grove et al. 2002, Table 5). This mixture was then melted using the melting reaction determined from the low-temperature wet H&Z+SM experiments. The rare earth element (REE) abundances of these calculated batch melts of the resulting metasomatized garnet lherzolite (open squares) are shown for 6, 10, 12 and 15 wt. % melting (Fig. 11), which are melting extents are similar to those measured in our near solidus experiments at temperatures below 1050^{o}C at 3.2 GPa. Batch melting was modeled using the appropriate equations from Shaw (2006) and partition coefficients from Halliday et al. (1995).

For comparison, the REE compositions (solid black symbols) of primitive Mount Shasta region basaltic andesites and primitive magnesian andesites (Grove et al., 2002) are also shown on Figure 11, along with the calculated composition of an added fluid-rich subduction zone silicate melt component (grey symbols) from Grove et al. (2002). Grove et al. (2002) calculated this "fluid-rich" melt component by estimating the trace and REE that could be contributed from 20-30% melt of depleted harzburgite residue and then used the pre-eruptive H_2O content of the primitive lavas to estimate the abundances of the trace elements added from whatever component conveyed the H_2O from the slab to the metasomatized mantle wedge.

Note the strong resemblance between the calculated REE abundances in the hydrous melts of metasomatized garnet lherzolite and the Grove et al. (2002) fluid-rich components. Both are depleted in heavy REE in the classic strongly sloping REE patterns from Gd to Yb. From these similarities in REE, we infer that one component of the primitive Mt. Shasta lavas is a hydrous silicate melt of metasomatized mantle formed in the presence of garnet that comes from deep in the mantle wedge, just above the slab – wedge interface.

In their discussion of the elemental characteristics of the fluid-rich melt component that was added to the primitive lavas from Mt. Shasta, Grove et al. (2002) also noted that the primitive magnesian andesites from Kamchatka and Setouchi also share REE characteristics with the Mt. Shasta region lavas. The chondrite normalized abundances of the primitive lavas from these two arcs are shown in Figure 12 along with the range of REE abundances found in the Mt. Shasta primitive lavas. While it is beyond the scope of this paper to infer the deep, fluid-rich contribution at these two arcs, it is clear that the REE abundances in these other arcs show the contribution of a low-degree partial melt which we suggest is also from melting of hydrous, metasomatized garnet lherzolite near the slab-wedge interface.

It is interesting to note that there also appears to be a spectrum of REE abundances in the fluid-rich melt component of the Shasta primitive lavas, which might be explained by mixing the deeper garnet-saturated lherzolite melts with shallower spinel-saturated lherzolite melts. To fully describe the major and trace element compositions of the Shasta primitive lavas, these hydrous melt components must be mixed with melts derived from depleted harzburgite source regions, presumably melted at shallower depths near the Moho. This shallow depth is consistent with all the phase equilibrium data that we have on the depths of last equilibration of primitive, hydrous subduction zone lavas (Mitchell and Grove, 2015; Grove et al., 2012; Gaetani and Grove, 2003), and suggest that trace elements preserve the processes of both initial deep melting as well as continued melting throughout pressure-temperature range of the mantle wedge, whereas the major elements dominantly record the last stage of melting and/or they partly re-equilibrate at the shallow depths of final melt segregation.

Conclusions

The first melts of hydrous lherzolite at pressures equivalent to those near the slab – wedge interface produce compositionally distinctive melts that are andesitic (58 – 60 wt. % SiO_2), but with low CaO contents (~1 wt. %). If these deep, hydrous melts are blended with hydrous mantle melts produced by shallow, high degree hydrous harzburgite melting, these experimentally-produced melts bracket the major element compositional variability observed in primitive high magnesian arc andesites and basaltic andesites. This process is schematically illustrated in Figure 13. Therefore, we suggest that these hydrous arc magmas form over a range of depths that begins at the base of the mantle wedge and ends at shallow mantle depths. The starting mantle that produces this match contains a metasomatic component (Grove et al., 2002) that one can think of as a "slab melt", but this component is a small proportion (~ 5 wt. %) and shows up as elevated alkalis ($Na_2O + K_2O$) in terms of their effect on the starting major element

composition of the mantle that undergoes melting. However, the contribution of this slab component to the REE and incompatible trace element budget is large, and we have shown that we can reproduce the trace elemental characteristics of the primitive andesites by adding a deep, low-degree hydrous melt. When we examine experiments that contain higher amounts a slab component (e.g. Mallik et al., 2015, with 25 wt. % slab melt), they do not resemble primitive high magnesian arc andesites and basaltic andesites. Models that invoke large components of added sediment or sediment melt will need to be calibrated by experiments performed at the appropriate conditions on appropriate bulk compositions such that they can reproduce both the major and trace element composition of primitive arc magmas, which has not been done to date. While we discuss only two sets of experiments and there are lots of pressure – temperature – mantle – slab component mixes that have been proposed to lead to the generation of arc andesites in subduction zone environments (e.g. Behn et al., 2011; Hacker et al., 2011; Kelemen and Behn, 2016), based on what we know now to date, it appears that melts mixes that consist of an alkali-and SiO_2-rich component (slab melt, sediment melt, sediment, etc.) to a mantle bulk composition will lead to the generation of alkali basalts, not magnesian andesite. Finally, we propose that the trace elements concentrations of primitive arc magmas preserve the processes of both initial deep, low % melts and extensive shallow hydrous melting. The major elements dominantly record the last stage of shallow melting (with the exception of CaO and K_2O), while the trace elements record evidence of the initial melting at depth in the mantle wedge. These shallow melts must be produced by a supply of H_2O with its slab component from deep (Fig. 13). At the same time early initial deep hydrous melts with their low CaO and elevated K_2O abundances must rise through the wedge without re-equilibrating and mixing at the shallow depths of final melt segregation, supporting at least some evidence of channelized flow in the mantle wedge at subduction zones.

Acknowledgements. This research was supported by NSF Grants EAR 1551321 to TLG and EAR 1447342 to CBT. We thank Peter Ulmer and an anonymous reviewer for their constructive reviews, along with Othmar Müntener for his editorial handling of the manuscript.

References

Armstrong JT (1995) CITZAF -- a package of correction programs for the quantitative electron microbeam X-ray analysis of thick polished materials, thin-films, and particles Microbeam Analysis 4:177-200

Baker MB, Stolper E (1994) Determining the composition of high-pressure mantle melts using diamond aggregates Geochimica et Cosmochimica Acta 58:2811-2827

Behn MD, Kelemen PB, Hirth G, Hacker BR, Massonne HJ (2011) Diapirs as the source of the sediment signature in arc lavas Nature Geoscience 4:641-646 doi:10.1038/ngeo1214

Boyd FR, England JL (1960) Apparatus for phase equilibrium studies at pressures up to 50 kilobars and temperatures up to 1750°C J Geophys Res 65:741-748

Brown SM, Behn MD, Grove TL (2019) The myth of garnet signatures and the origin of plagioclase signatures in mid-ocean ridge basalts J Geophys Res (submitted)

Bryant JA, Yogodzinski GM, Churikova TG (2011) High-Mg# andesitic lavas of the Shisheisky Complex, Northern Kamchatka: implications for primitive calc-alkaline magmatism Contrib Mineral Petrol 161:791-810 doi:10.1007/s00410-010-0565-4

Davies JH, Stevenson DJ (1992) Physical Model of Source Region of Subduction Zone Volcanics J Geophys Res 97:2037-2070

Falloon TJ, Danyushevsky LV (2000) Melting of refractory mantle at 1.5, 2 and 2.5 GPa under, anhydrous and H2O-undersaturated conditions: Implications for the petrogenesis of high-Ca boninites and the influence of subduction components on mantle melting J Petrol 41:257-283

Gaetani GA, Grove TL (1998) The influence of water on melting of mantle peridotite Contrib Mineral Petrol 131:323-346

Gaetani GA, Grove TL (2003) Experimental constraints on melt generation within the mantle wedge. In: Eiler JM (ed) Geophysical Monograph 138: Inside the Subduction Factory, vol 136. American Geophysical Union, Washington, D.C., pp 107 - 134

Gill JB (1981) Orogenic Andesites and Plate Tectonics. Springer-Verlag, New York, New York

Green DH (1973) Experimental Melting Studies on a Model Upper Mantle Composition at High-Pressure under Water-Saturated and Water-Undersaturated Conditions Earth Planet Sci Lett 19:37-53

Green DH (1976) Experimental testing of "equilibrium" partial melting of peridotite under water-saturated, high-pressure conditions Canada Mineral 14:255-268

Green DH, Hibberson WO, Kovacs I, Rosenthal A (2010) Water and its influence on the lithosphere-asthenosphere boundary Nature 467:448-451

Green DH, Hibberson WO, Rosenthal A, Kovacs I, Yaxley GM, Falloon TJ, Brink F (2014) Experimental Study of the Influence of Water on Melting and Phase Assemblages in the Upper Mantle J Petrol 55:2067-2096 doi:10.1093/petrology/egu050

Grove TL, Chatterjee N, Parman SW, Medard E (2006) The influence of H_2O on mantle wedge melting Earth Planet Sci Lett 249:74-89 doi:10.1016/j.epsl.2006.06.043|ISSN 0012-821X

Grove TL, Holbig ES, Barr JA, Till CB, Krawczynski MJ (2013) Melts of garnet lherzolite: Experiments, models and comparison to melts of ganet pyroxenit and carbonated lherzolite Contrib Mineral Petrol 166:887-910 doi: 1007/s00410-013-0899-9

Grove TL, Parman SW (2004) Thermal evolution of the Earth as recorded by komatiites Earth Planet Sci Lett 219:173-187

Grove TL, Parman SW, Bowring SA, Price RC, Baker MB (2002) The role of an H2O-rich fluid component in the generation of primitive basaltic andesites and andesites from the Mt. Shasta region, N California Contrib Mineral Petrol 142:375-396

Grove TL, Till CB, Krawczynski MJ (2012) The Role of H2O in Subduction Zone Magmatism. In: Jeanloz R (ed) Annual Review of Earth and Planetary Sciences, Vol 40, vol 40. Annual Review of Earth and Planetary Sciences. pp 413-439. doi:10.1146/annurev-earth-042711-105310

Hacker BR, Kelemen PB, Behn MD (2011) Differentiation of the continental crust by relamination Earth Planet Sci Lett 307:501-516 doi:10.1016/j.epsl.2011.05.024

Halliday AN, Lee D-C, Tommasini S, Davies GR, Paslick CR, Fitton JG, James DE (1995) Incompatible trace elements in OIB and MORB and source enrichment in the sub-oceanic mantle Earth Planet Sci Lett 133:379-395

Hart SR, Zindler A (1986) In search of a bulk-Earth composition Chem Geol 57:247-267

Hattori KH, Wallis S, Enami M, Mizukami T (2009) Subduction of mantle wedge peridotites: Evidence from the Higashi-akaishi ultramafic body in the Sanbagawa metamorphic belt Island Arc 19:192-207 doi:10.1111/j.1440-1738.2009.00696.x

Hays JF (1966) Lime-alumina-silica Carnegie Institution of Washington Year Book:234-239

Hoffman AW (1988) Chemical differentiation of the Earth: the relationship between mantle, continental crust, and oceanic crust Earth Planet Sci Lett 90:297-314

Johannes W et al. (1971) An interlaboratory comparison of piston-cylinder pressure calibration using the albite-breakdown reaction Contrib Mineral Petrol 32:24-38

Kelemen PB, Behn MD (2016) Formation of lower continental crust by relamination of buoyant arc lavas and plutons Nature Geoscience 9:197-205 doi:10.1038/ngeo2662

Kinzler RJ (1997) Melting of mantle peridotite at pressures approaching the spinel to garnet transition: Application to mid-ocean ridge basalt petrogenesis J Geophys Res 102:853-874

Kushiro I (1968) Compositions of magmas formed by partial zone melting of the Earth's upper mantle J Geophys Res 73:619-634

Kushiro I (1972) Effect of water on the composition of magmas formed at high pressures J Petrol 13:311-334

Kushiro I, Syono Y, Akimoto S (1968) Melting of a peridotite nodule at high pressures and high water pressures Journal of Geophysical Research, B, Solid Earth & Planets 73:6023-6029

Kushiro I, Walter MJ (1998) Mg-Fe partitioning between olivine and mafic-ultramafic melts Geophys Res L 25:2337-2340

Longhi J (2005) Temporal stability and pressure calibration of barium carbonate and talc/pyrex pressure media in a piston-cylinder apparatus Am Mineral 90:206-218

Mallik A, Nelson J, Dasgupta R (2015) Partial melting of fertile peridotite fluxed by hydrous rhyolitic melt at 2-3 GPa: implications for mantle wedge hybridization by sediment melt and generation of ultrapotassic magmas in convergent margins Contrib Mineral Petrol 169 doi:10.1007/s00410-015-1139-2

Mandler B, Grove TL (2016) Controls on the stability and composition of amphibole in the Earth's mantle Contrib Mineral Petrol 171 doi:10.1007/s00410-016-1281-5

Medard E, Grove TL (2008) The effect of H2O on the olivine liquidus of basaltic melts: experiments and thermodynamic models Contrib Mineral Petrol 155:417-432

Mitchell AL, Grove TL (2015) Melting the hydrous, subarc mantle: the origin of primitive andesites Contrib Mineral Petrol 170 doi:10.1007/s00410-015-1161-4

Mysen BO (1975) Partitioning of iron and magnesium between crystals and partial melts in peridotite upper mantle Contrib Mineral Petrol 52: 69-76

Mysen BO, Boettcher AL (1975a) Melting of a Hydrous Mantle : I. Phase Relations of Natural Peridotite at High-Pressures and Temperatures with Controlled Activities of Water, Carbon-Dioxide, and Hydrogen J Petrol 16:520-548

Mysen BO, Boettcher AL (1975b) Melting of a Hydrous Mantle :II. Geochemistry of Crystals and Liquids Formed by Anatexis of Mantle Peridotite at High Pressures and High Temperatures as a Function of Controlled Activities of Water, Hydrogen and Carbon Dioxide J Petrol 16:549-593

Nehru CE, Wyllie PJ (1975) Compositions of Glasses from St. Paul's Peridotite Partially Melted at 20 kilobars J Geol 83:455-471

Poldervaart A (1955) Chemistry of the Earth's crust Geological Society of America Special Paper 2:119-144

Roeder P, Emslie R (1970) Olivine-liquid equilibrium Contrib Mineral Petrol 29:275-289

Shaw DM (2006) Trace elements in magmas: a theoretical treatment. Cambridge University Press, Cambridge

Tatsumi Y, Hamilton DL, Nesbitt RW (1986) Chemical Characteristics of Fluid Phase Released from a Subducted Lithosphere and Origin of Arc Magmas - Evidence from High-Pressure Experiments and Natural Rocks J Volcan Geotherm Res 29:293-309

Tatsumi Y, Ishizaka K (1982) Origin of High-Magnesian Andesites in the Setouchi Volcanic Belt, Southwest Japan .1. Petrographical and Chemical Characteristics Earth Planet Sci Lett 60:293-304 doi:10.1016/0012-821x(82)90008-5

Tenner TJ, Hirschmann MM, Humayun M (2012) The effect of H2O on partial melting of garnet peridotite at 3.5 GPa Geochem Geophys Geosyst 13 doi:Q03016/10.1029/2011gc003942

Till CB (2017) A review and update of mantle thermobarometry for primitive arc magmas Am Mineral 102:931-947 doi:10.2138/am-2017-5783

Till CB, Carlson RW, Grove TL, Wallis S, Mizukami T (2009) A missing link in understanding mantle wedge melting, Higashi-akaishi peridotite, Japan EOS, AGU Fall Meeting abstract V44A-03

Till CB, Grove TL, Withers AC (2012) The Beginnings of Hydrous Mantle Wedge Melting Contributions to Mineralogy and Petrology 163:669–688 DOI 10.1007/s00410-011-0692-6

Toplis MJ (2005) The thermodynamics of iron and magnesium partitioning between olivine and liquid: criteria for assessing and predicting equilibrium in natural and experimental systems Contrib Mineral Petrol 149:22-39

Ulmer P (1989) The Dependence of the Fe-2+-Mg Cation-Partitioning between Olivine and Basaltic Liquid on Pressure, Temperature and Composition - an Experimental-Study to 30 Kbars Contrib Mineral Petrol 101:261-273

Walter MJ (1998) Melting of Garnet Peridotite and the Origin of Komatiite and Depleted Lithosphere J Petrol 39:29-60

Watson EB, Wark DA, Price JD, Van Orman JA (2002) Mapping the thermal structure of solid-media pressure assemblies Contrib Mineral Petrol 142:640-652

White BS, Wyllie PJ (1992) Solidus reactions in synthetic lherzolite-H2O-CO2 from 20-30 kbar, with applications to melting and metasomatism J Volcan Geotherm Res 50:117-130 doi:10.1016/0377-0273(92)90040-k

Figure Captions

Figure 1. Temperature and phase assemblages in the 3.2 GPa experiments discussed in this paper. Left hand side shows the experiments performed on the H&Z + SM compositions (4 wt. % H_2O) from Mitchell and Grove (2015). All experiments contained olivine + orthopyroxene + clinopyroxene + garnet + melt. Additionally, experiments at temperatures below 950 ^oC contained rutile. The right hand side shows the H&Z + H2O composition experiments reported in Till et al. (2012) (14.5 wt. % H_2O). Mineral phase compositions are presented in Till et al. (2012). Liquid compositions were reanalyzed and are reported in this study. Experiments at 1125 and 1150 ^oC contained olivine + orthopyroxene + spinel + melt. All others contained olivine + orthopyroxene + clinopyroxene + garnet + melt. On the right are the hydrous solidus temperatures at 3.2 GPa reported by other studies.

Figure 2. Backscattered Electron (BSE) images of selected experiments showing the textural relationships and melt distribution (see supplementary Figure 1 for BSE images of all the H&Z +SM experiments). In all images the bright white is the enclosing Au capsule and a scale bar equal to 100 microns is shown for each image. A.) Experiment D287, 1150 ^oC, 3.2 GPa. The top (hot end) of the experimental charge is toward the top of the figure. Quench-modified melt phase is evident on the left side of the image. B.) Experiment D276, 1075 ^oC, 3.2 GPa. The top (hot end) of the experimental charge is toward the left of the figure. Quench-modified melt phase is evident on the left side of the image. C.) Experiment D287, 1000 ^oC, 3.2 GPa. The top (hot end) of the experimental charge is toward the top of the figure. Regions of quench-modified melt phase are just below and above the tongue of Au that was folded into the capsule when it was shortened during preparation. The larger mineral grains in each charge (50 to 200 microns in diameter) are garnet crystals that poikilitcally enclose finer grained (10 – 20 micron) olivine, orthopyroxene and clinopyroxene crystals.

Figure 3. Changes in texture and distribution of the quench-modified melt phase of selected experiments in Backscattered Electron (BSE) image mode (see supplementary materials for similar BSE images of all the H&Z +SM experiments). A.) Experiment D287, 1150 ^oC, 3.2 GPa. Note sheet-like habit of quench-modified melt (dark) and intergrown quench crystals (light patches). B.) Experiment D255, 1050 ^oC, 3.2 GPa, Upper corner of charge has been filled with epoxy (dark background surrounded by Au capsule). Within epoxy micron-thick sheets of quench-modified andesitic glass have been preserved. Also present are light colored 2-3 micron spheres of granitic melt phase. 10-30 micron wide crystals are present on right side of image. C.) Experiment D250, 1000 ^oC, 3.2 GPa. In this corner of the charge the melt phase has been partly plucked out, and is preserved as thin sheets that blanket the 10 – 30 micron enclosing crystals. Micron-sized spheres of granite are also present. D.) Experiment D260, 950 ^oC, 3.2 GPa. As in B), the upper corner of charge has been filled with epoxy and preserves micron-thick sheets of quench-modified andesitic glass and light colored 2-3 micron spheres of granitic component.

Figure 4. Close up view of the quench-modified andesitic melt sheets and spheres of granitic melts in D255 (Fig. 2B) in Backscattered Electron image mode (A, COMP) and Secondary Electron Image (B, SEI) mode. White region on left in the COMP image is the Au capsule. The area to the right has been partly filled by epoxy and preserves the delicate andesitic melt sheets that form when H_2O exsolves from the melt phase on quench. The expansion of the melt separates the crystals (oliv, and top of charge) and the presence of a super-critical fluid is evidenced by the presence of vesicles in the melt (B, comp). The fluid in these vesicles precipitates a spherical silicate component upon quench that is granitic in composition. The vesicle is surrounded by the andesitic melt sheets and the 3-dimensional nature of the melt sheets can be seen in the SEI image where the sheets fold up and over at the edge of the granite-sphere

lined vesicle. Tot the right of the labeled oliv crystal in both COMP and SEI images a tangle of the andesitic melt sheets is visible. Three other holes are visible in the SEI image and these are the broken tops of andesitic melt that surrounded the fluid-phase.

Figure 5. Compositions of experimentally-produced liquids from hydrous lherzolite melting experiments plotted as oxide wt. % vs. temperature (in ^{o}C). Liquids produced from the H&Z + SM composition (4 wt. % H_2O) are shown as black squares with the coexisting high silica spheres shown as open squares. Liquids produced from the H&Z + H2O composition (14.5 wt. % H_2O) are shown as black circles. Experiments reported by Mysen and Boettcher (1975) (5 wt. % H_2O) at 1.5 GPa are shown as light grey diamonds, and the two experimental liquids reported in Green et al. (2014) are shown s dark grey diamonds. A). SiO_2 vs. T. B) Al_2O_3 vs. T. C.) MgO vs. T. D.) FeO vs. T. E.) CaO vs. T. F.) Na_2O vs. T.

Figure 6. Pseudoternary subprojections for the pseudoquaternary system Olivine – Clinopyroxene – Garnet – Quartz in oxygen units (see supplementary Table 1 for calculation scheme) showing compositions of experimentally produced liquids from hydrous lherzolite melting experiments in Fig. 5.

Figure 7. Oxide – oxide variation diagrams of experimentally produced liquids from hydrous lherzolite melting experiments and calculated 3.2 GPa anhydrous garnet lherzolite melts from Grove et al. (20-13) and Brown et al., 2019). See figure 5 for symbol explanation. Additional experimental data included here are from Gaetani et al. (1998) (dark grey triangles), Tenner et al. (2012) (open triangles), Mallik et al. (2015) (light grey triangles) and natural primitive lavas reported in Mitchell and Grove (2015) (light grey stars). A). MgO vs. SiO_2. B) FeO vs. SiO_2. C.) Al_2O_3 vs. SiO_2. D.) CaO vs. SiO_2. E.) Na_2O vs. SiO_2. F.) K_2O vs. SiO_2. Calculated garnet lherzolite batch melts cover the range from 1 to 10 wt. %. Compositions are presented in supplementary Table 6.

Figure 8. Pseudoternary subprojections for the pseudoquaternary system Olivine – Clinopyroxene – Garnet – Quartz in oxygen units showing compositions of experimentally produced liquids from hydrous lherzolite melting experiments and calculated anhydrous garnet lherzolite melts shown in Fig. 7. Note that one Green point and two Mallik points plot at highly negative Qtz values on Oliv – Garnet – Qtz, so they are not shown.

Figure 9. Oxide – oxide variation diagrams of experimentally produced liquids from hydrous lherzolite melting experiments. Along with the first melts of hydrous lherzolite reported in this study are experimentally produced high extent melts in equilibrium with harzburgite residues from Mitchell and Grove (2015). These are compared with the natural primitive lavas reported in Mitchell and Grove (2015) and shown in Figures 7 and 8 as grey stars. Here they are separated by arc. The blue diamonds labeled Cascades are Mt. Shasta primitive basaltic andesites and magnesian andesites from Grove et al. (2002). Red diamonds are lavas from Setouchi, Japan (Tatsumi and Ishikawa, 1982). Orange diamonds are samples from Kamchatka (Bryant et al., 2010). A). MgO vs. SiO_2. B) FeO vs. SiO_2. C.) Al_2O_3 vs. SiO_2. D.) CaO vs. SiO_2. E.) Na_2O vs. SiO_2. F.) K_2O vs. SiO_2.

Figure 10. Change in melt producing reaction illustrated in the Olivine – Garnet – Quartz subprojection of the pseudoquaternary Olivine – Clinopyroxene – Garnet – Quartz in oxygen units (see supplementary Table 5). At low temperature end the melt is quartz- and corundum-normative and the melt reaction is peritectic with garnet + opx + cps meting to olivine + liquid.

At the high temperature end the hydrous melts become silica-undersaturated and the peritectic reaction changes to garnet + oliv + cpx = liquid + opx.

Figure 11. Chondrite normalized rare earth element (REE) abundances of low degree melts of hydrous metasomatized garnet lherzolite using the melting reaction obtained from the H&Z + SM experiments and a starting composition composed of 90 % primitive lherzolite (Hoffman ,1988) plus 10 % of an eclogite slab component (Grove et al., 2002) at 6 and 10 wt. % melting (open squares). These model melt compositions are compared with REE compositions (solid black symbols) of primitive Mount Shasta region basaltic andesites and primitive magnesian andesites (Grove et al., 2002, see text for symbol explanations) and the composition of the predicted fluid-rich silicate melt component estimated by Grove et al. (2002).

Figure 12. Chondrite normalized rare earth element (REE) abundances of primitive magnesian andesites from the Setouchi, Japan arc (Tatsumi and Ishikawa, 1982) and Kamchatka arc (Bryant et al., 2010) are compared with the range of REE abundance variations shown in the primitive Mt. Shasta lavas shown in Fig. 11 (light grey field).

Figure 13. Schematic model of the hydrous mantle melting processes that occur in the subduction zone setting. Melting begins at depths and temperatures just above the vapor-saturated solidus of a metasomatized garnet lherzolite source. The compositions of these deep, hydrous low-degree melts are provided by the hydrous 3.2 GPa experiments discussed in this paper. The melts are broadly andesitic (58 – 60 wt. % SiO_2) with very low CaO (~1 wt. %) and elevated K_2O (4-5 wt. %). These melts ascend into shallow, hot mantle, where they mix with high-extent hydrous melts of a harzburgite also produced by hydrous melting fluxed by a fluid-rich component transported from near the slab – wedge interface to form the primitive basaltic andesites and magnesian andesites found globally in arcs.

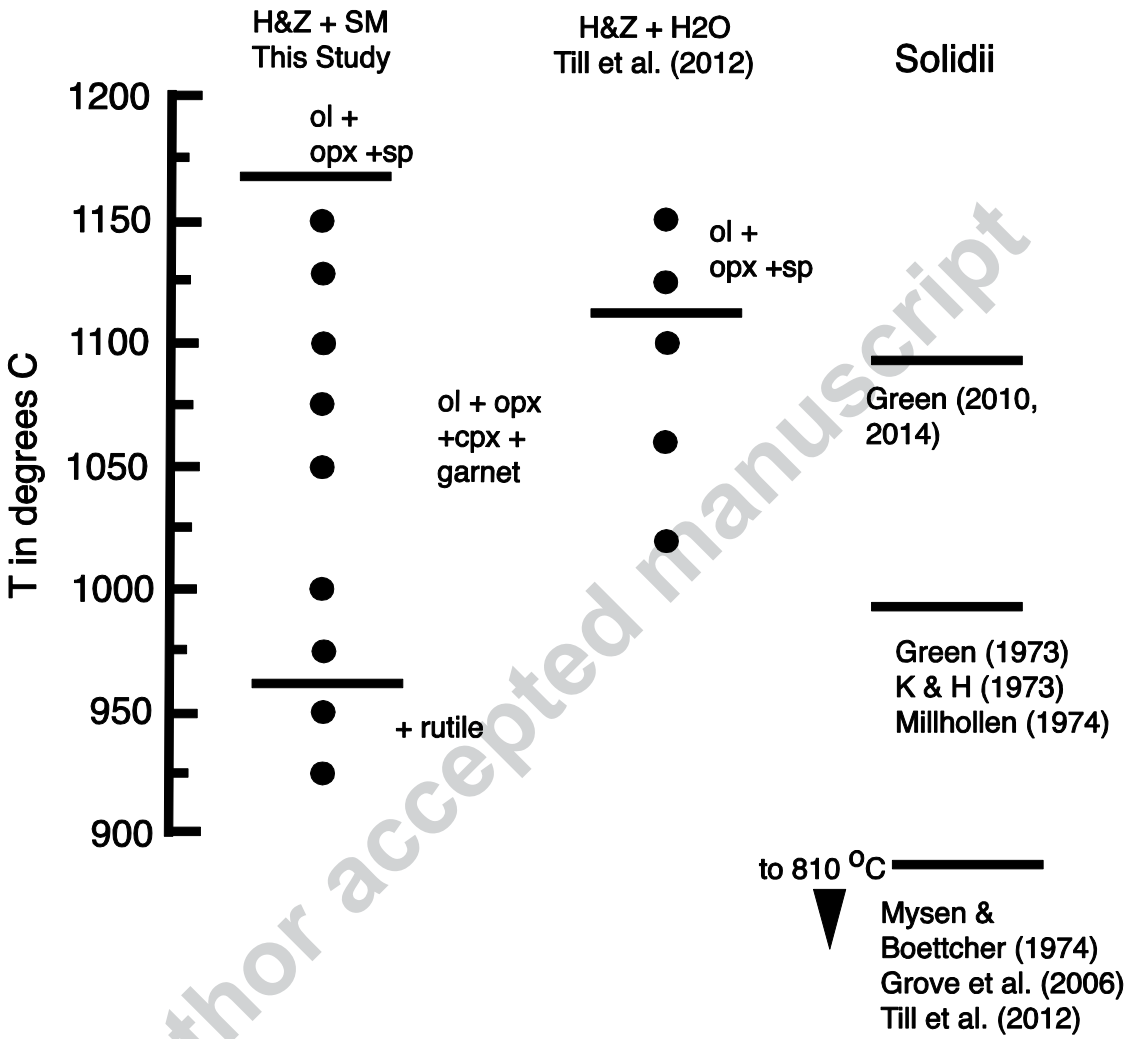

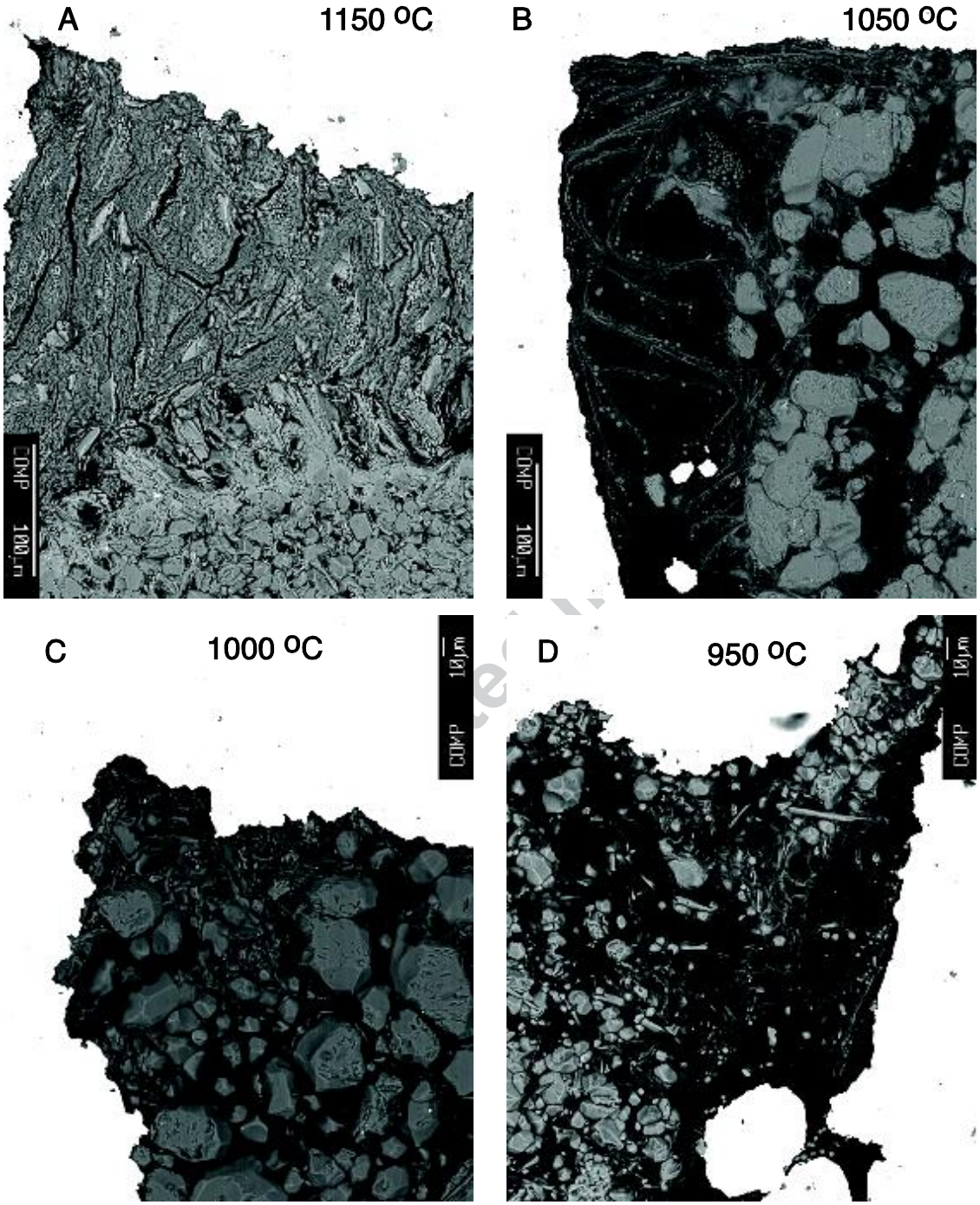

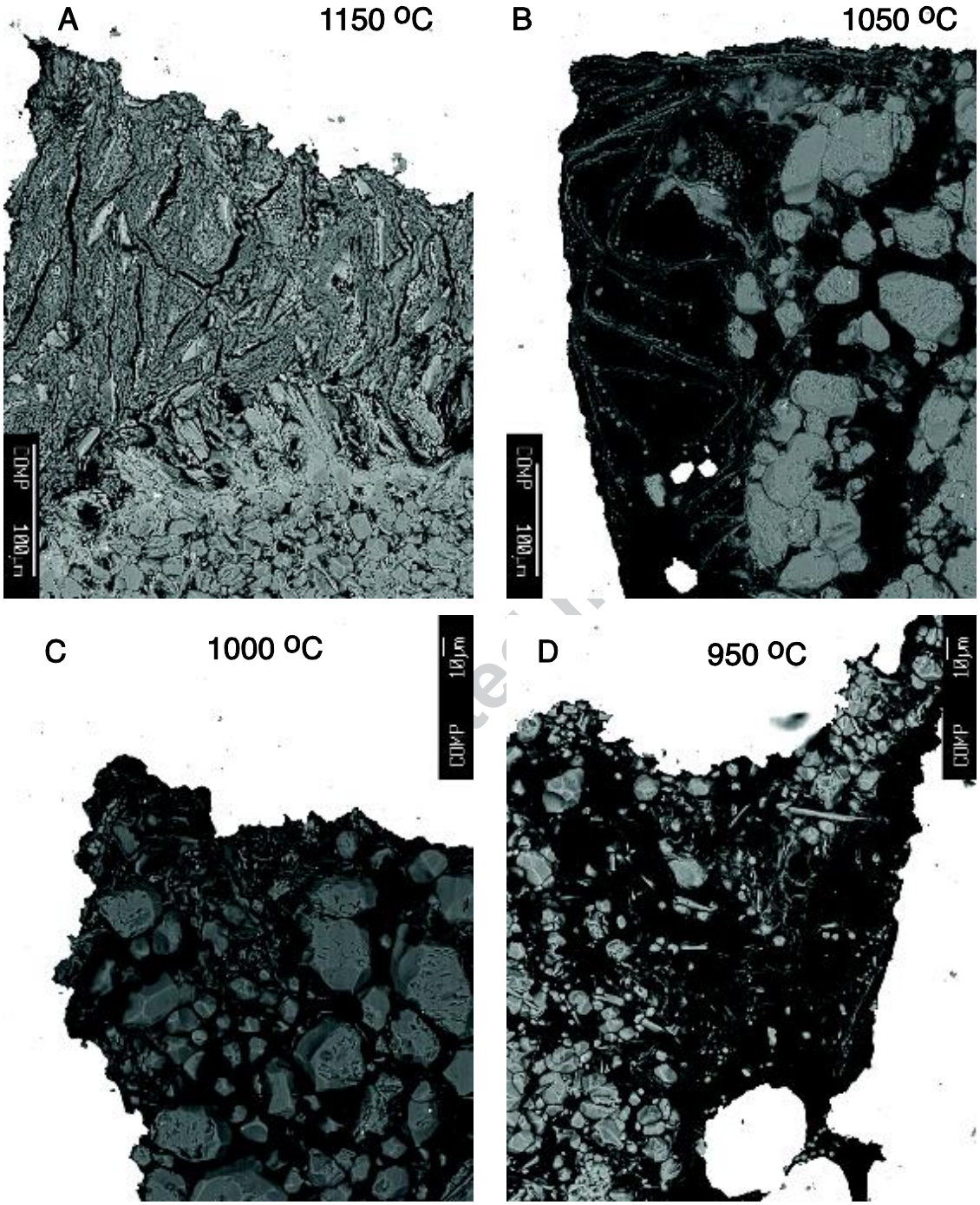

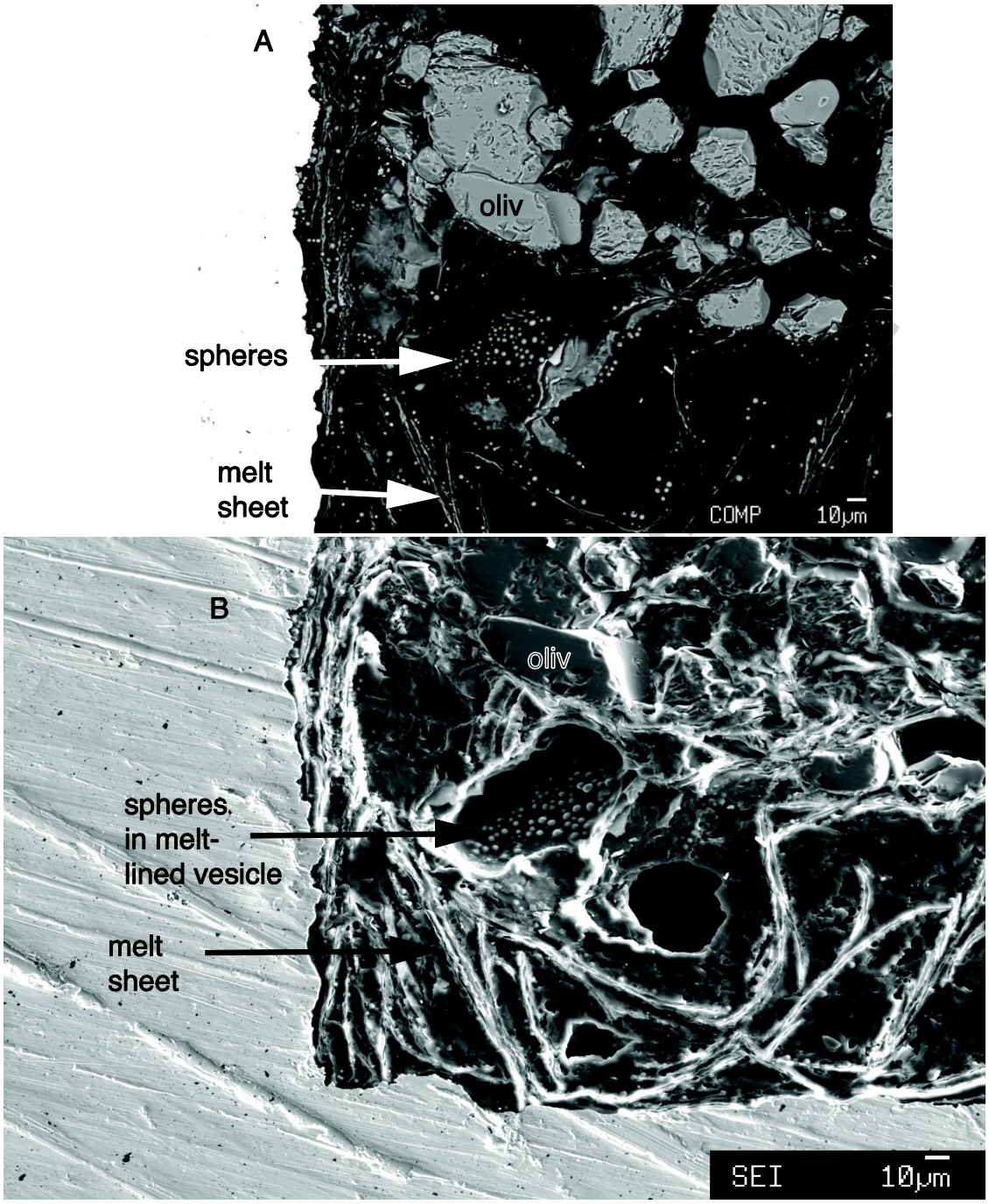

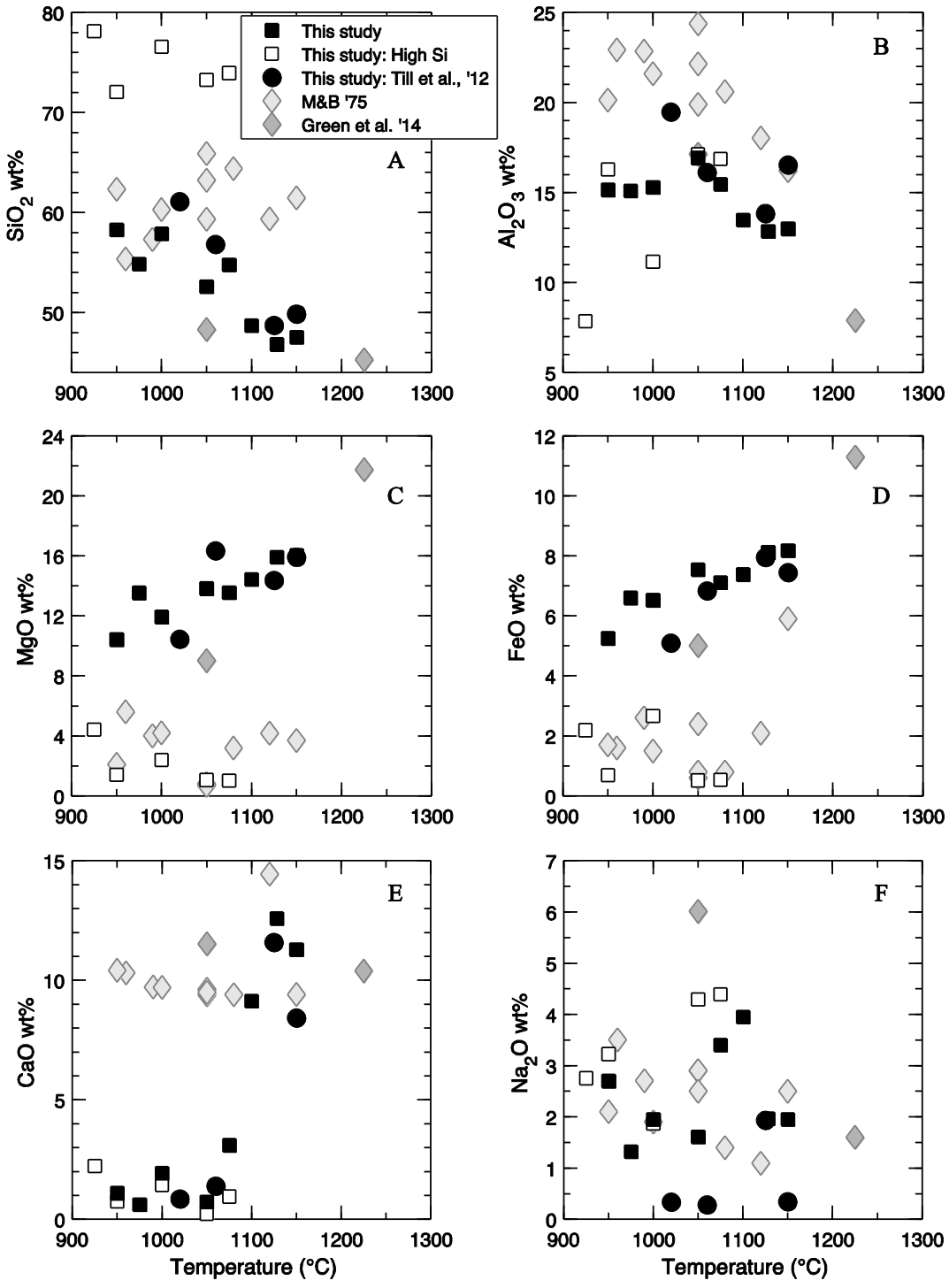

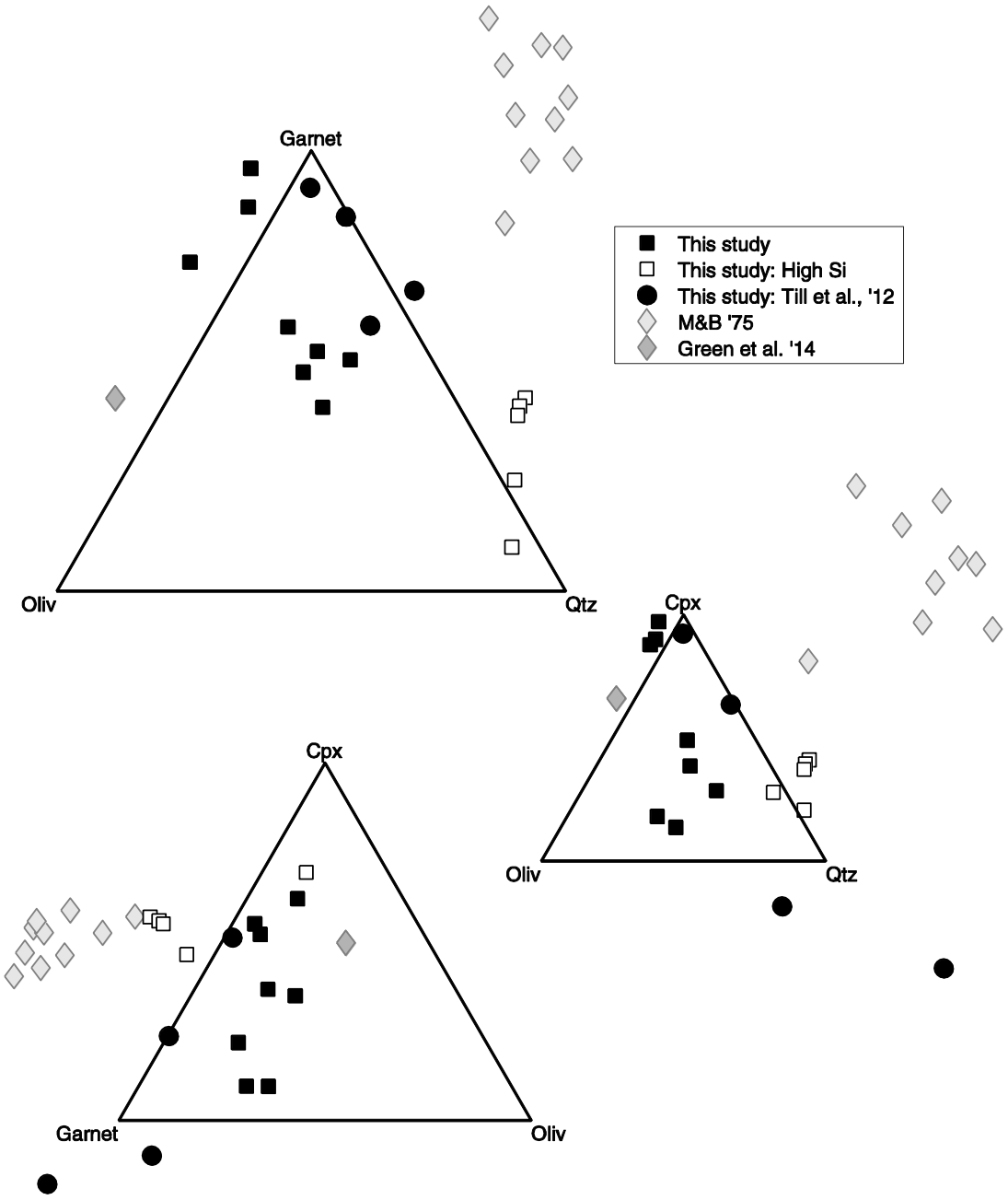

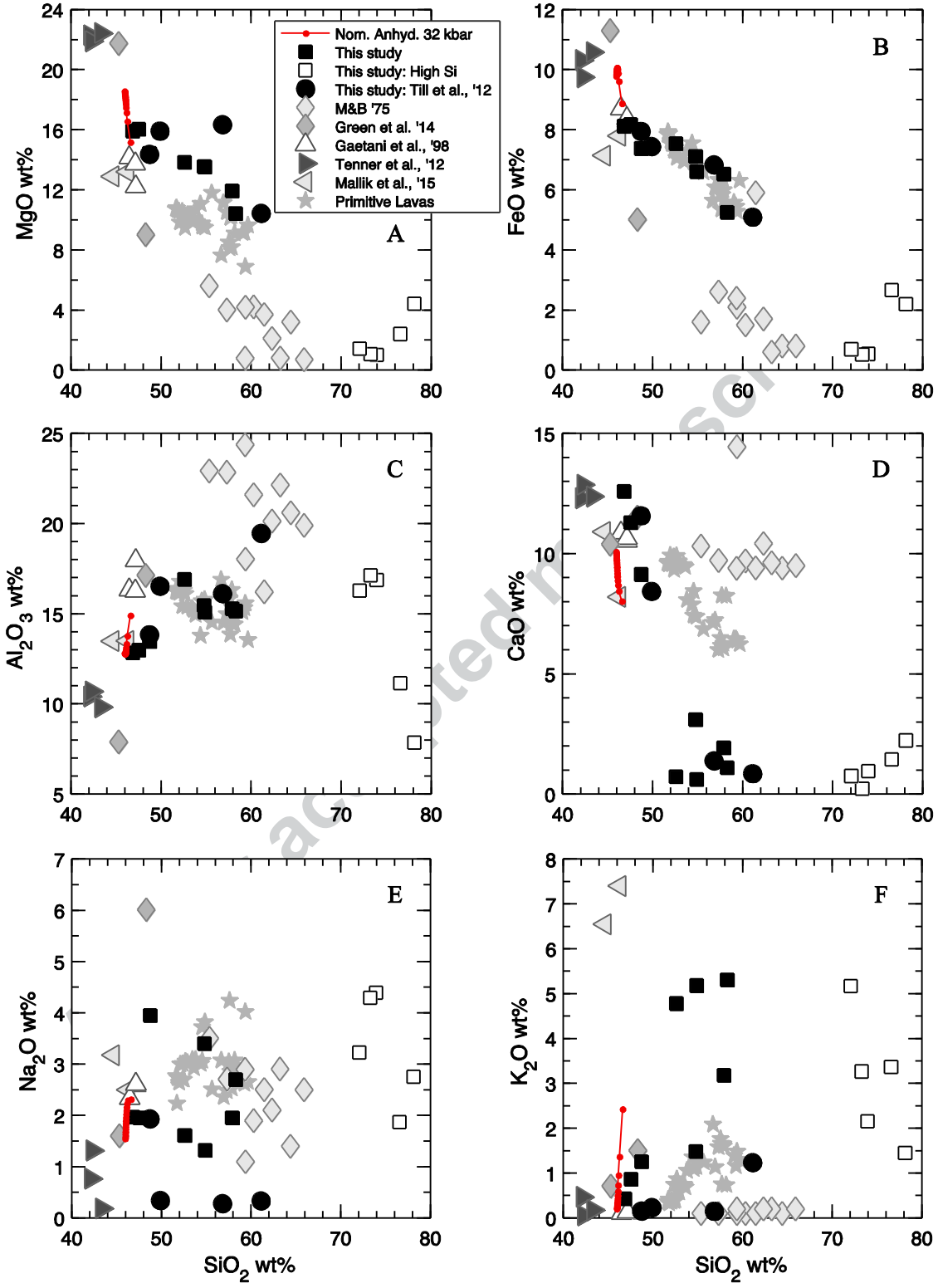

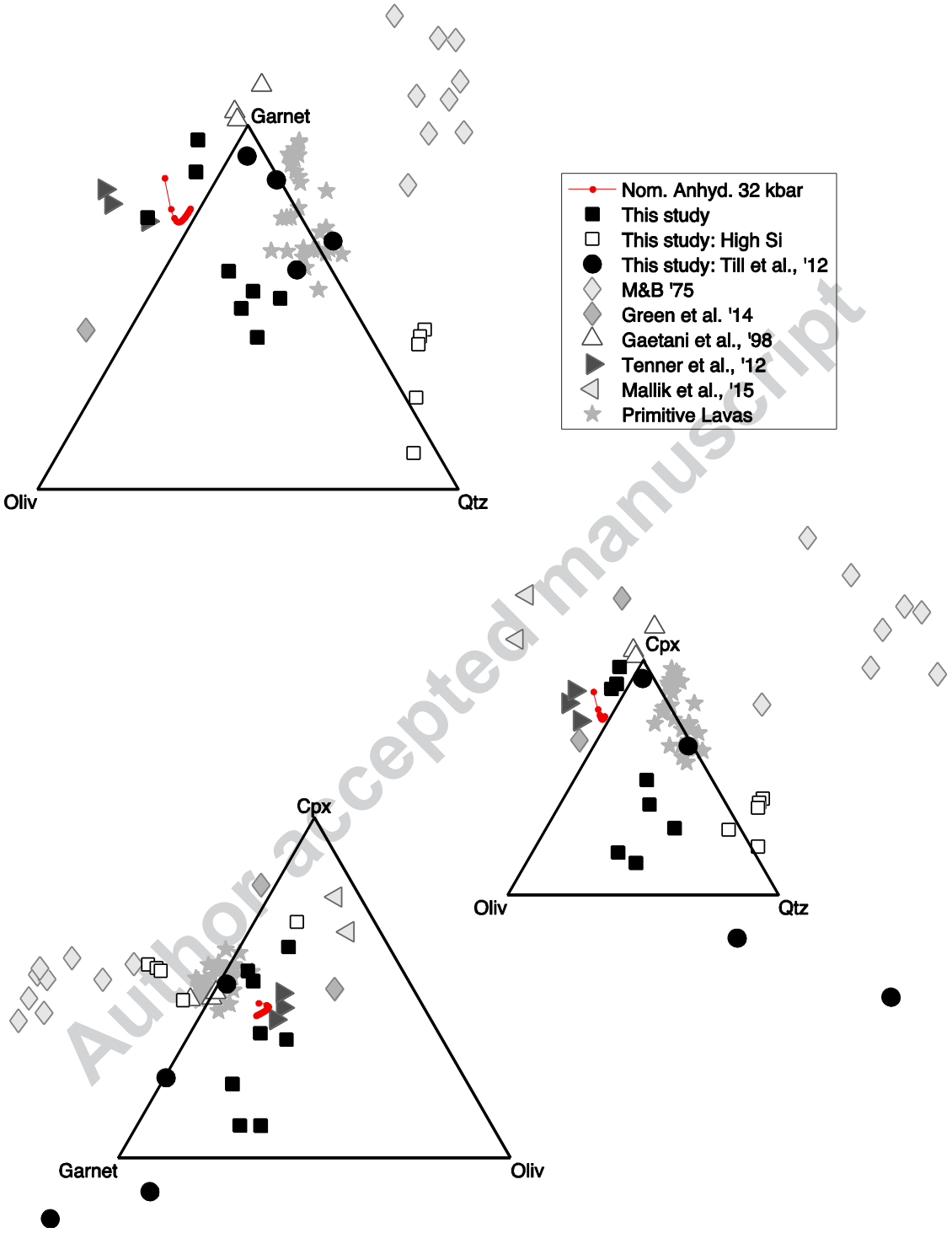

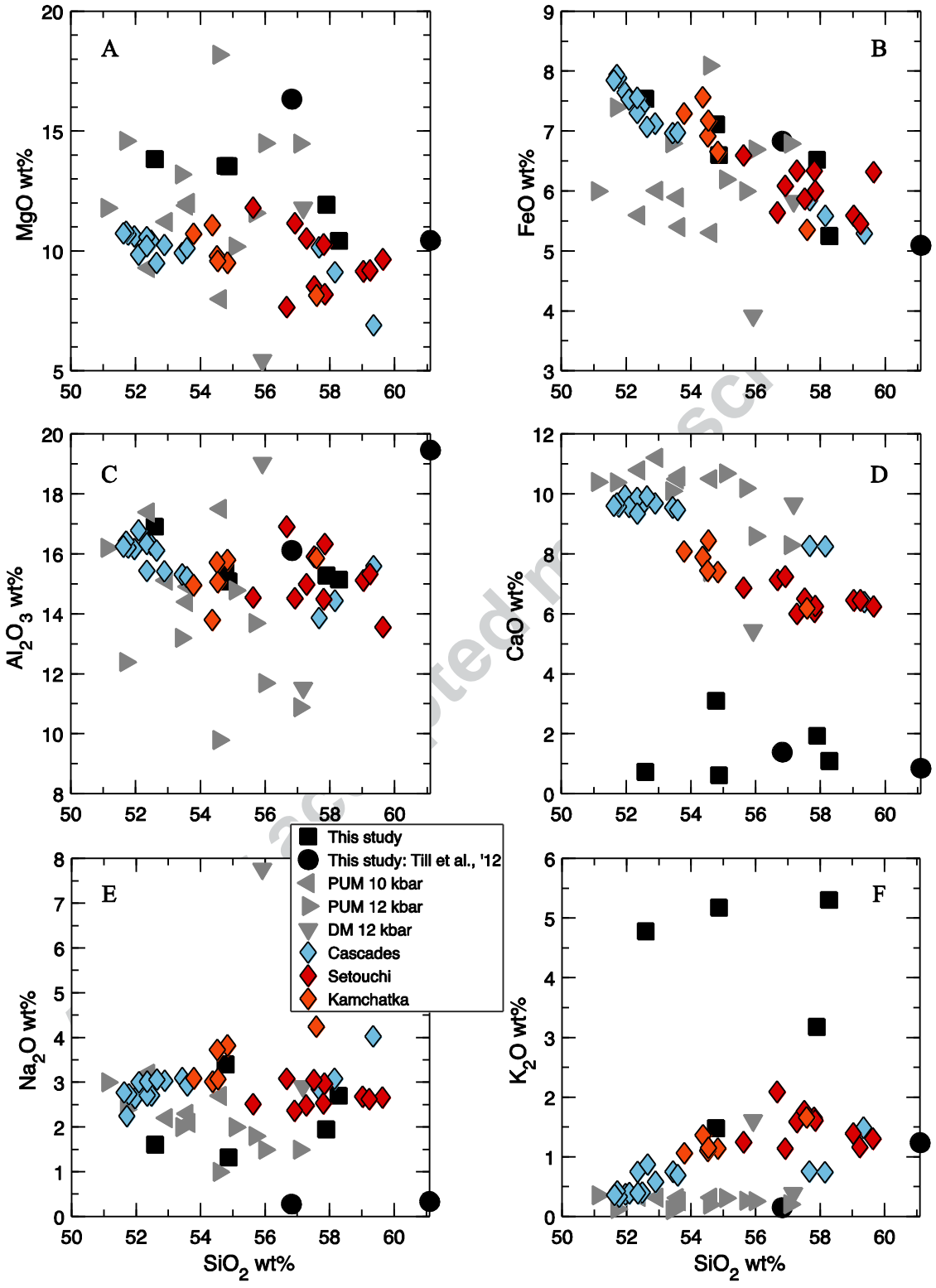

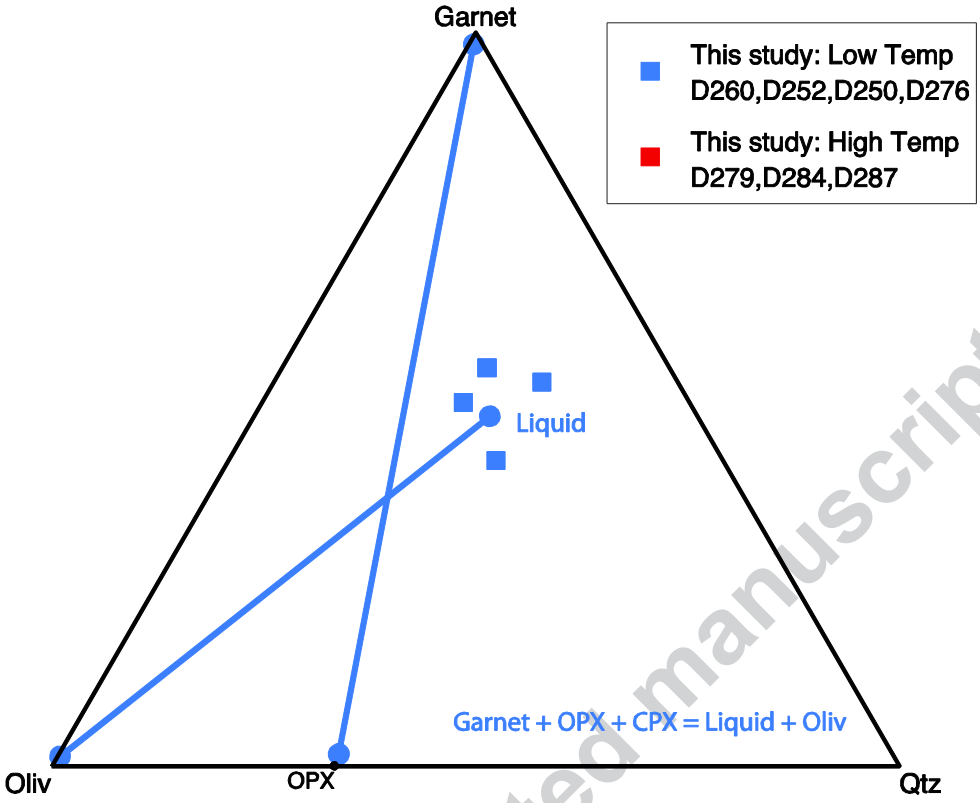

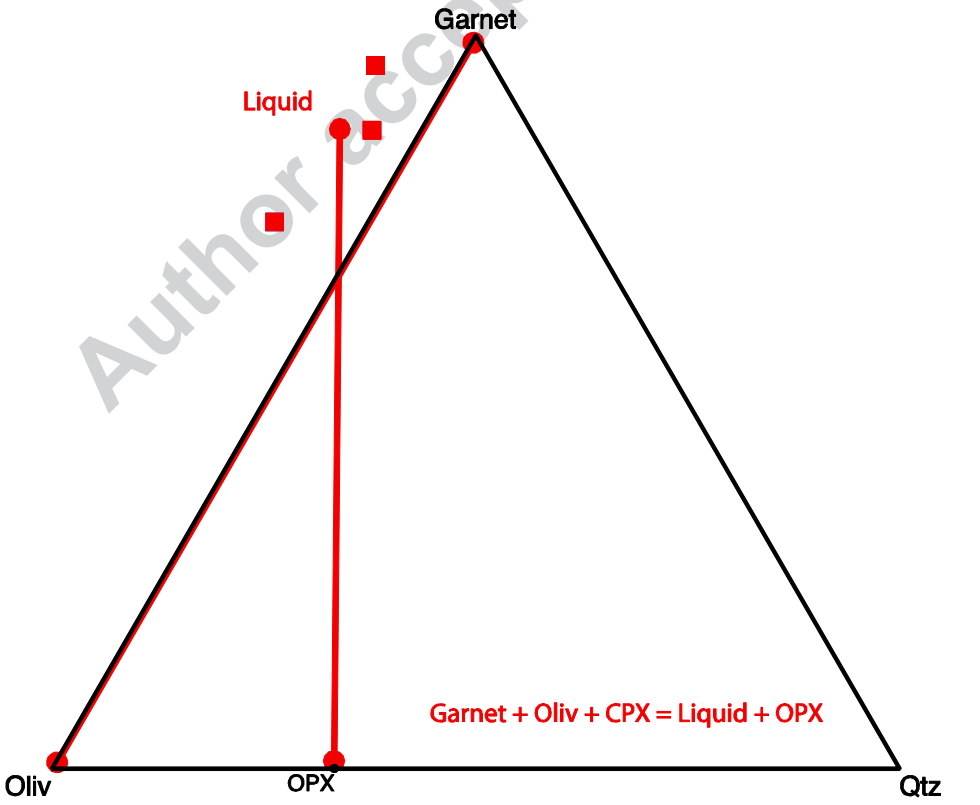

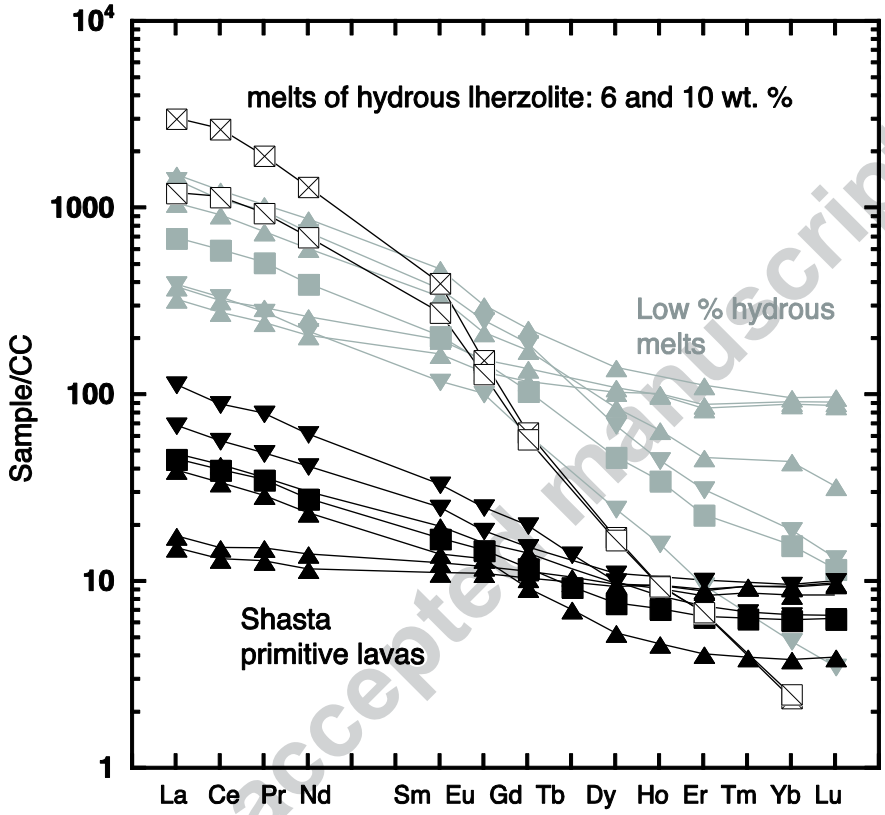

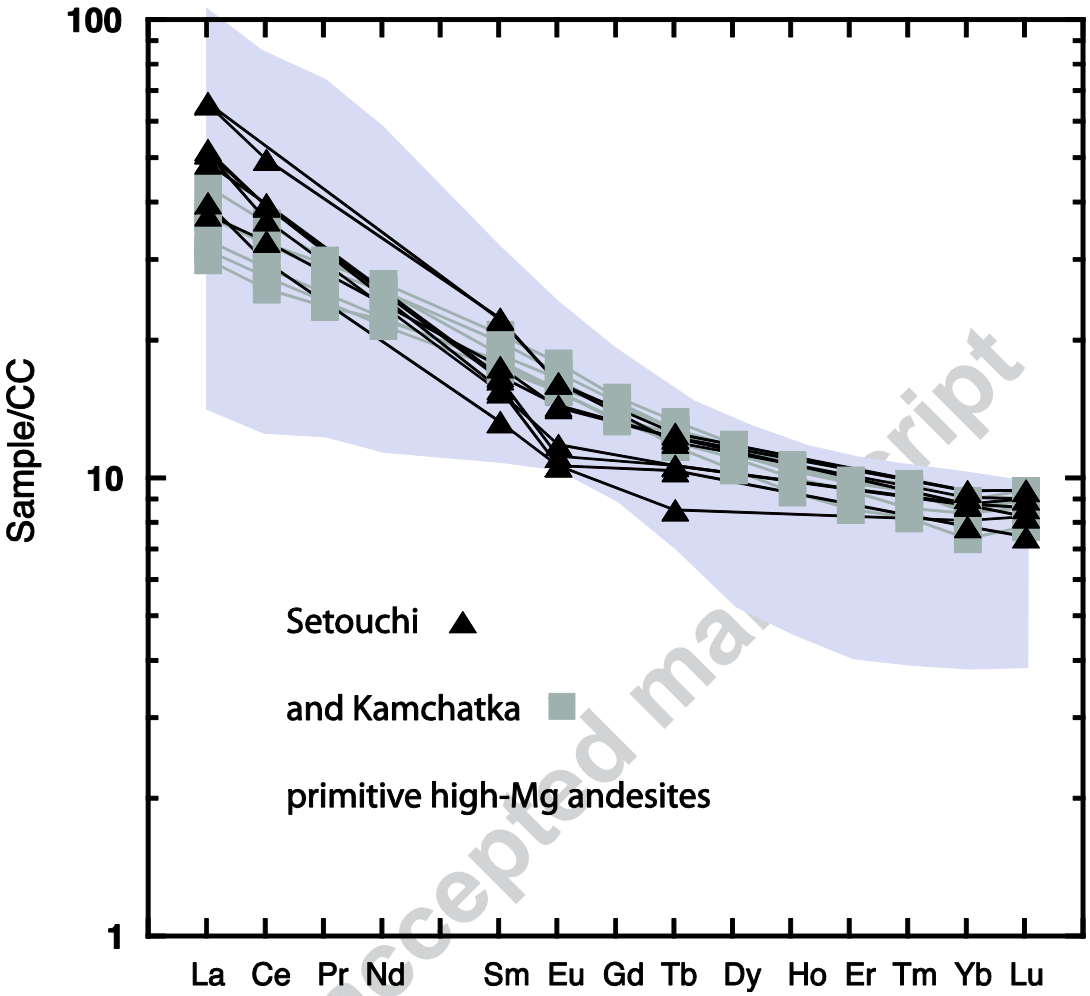

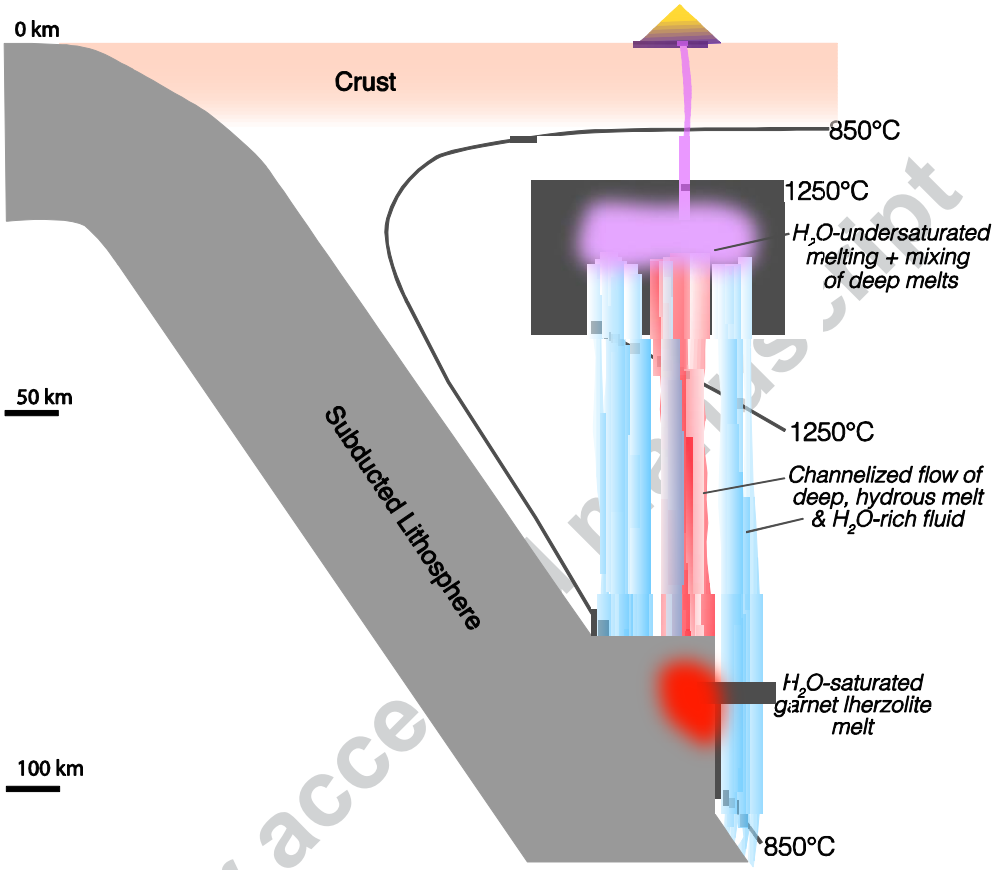

Table 1. Compositions used as starting material for the experiments. H&Z+H2O is from Til et al. (2011) a
(2015).
H2O denotes the amount of H2O added as Mg(OH)2.

	SiO2	TiO2	Al2O3	Cr2O3	FeO	MnC
H&Z+H2O	46.20	0.18	4.06	0.40	7.56	0.10
dry H&Z+SM	46.34	0.18	4.25	0.40	7.45	0.10
wet H&Z+SM	46.3	0.18	4.21	0.40	7.48	0.10

Table 2. Experimental run conditions and phases present. Mass calculati

Expt.	P (GPa)	T °C	Duration (hrs)	H2O present?	Phases ol	cpx	opx	gt
3 wt. % H2O Experiments (H&Z +SM starting material)								
D287	3.2	1150	68.5	yes	47.0 (0.4)	0.1 (0.1)	26.0 (0.7)	0.2 (
D284	3.2	1128	65.5	yes	45.1 (0.8)	0.1 (0.1)	28.6 (1.3)	3.7 (
D279	3.2	1100	196.6	yes	48.2 (0.6)	6.7 (0.6)	24.2 (0.9)	8.8 (
D276	3.2	1075	193.2	yes	54.9 (1.3)	9.8 (0.5)	16.9 (2.1)	10.6
D255	3.2	1050	138.0	yes	55.2 (4.2)	12.5 (1.5)	12.2 (6.8)	5.9 (
D250	3.2	1000	143.8	yes	51.9 (3.3)	10.8 (0.9)	17.8 (5.1)	10.8
D252	3.2	975	336.7	yes	55.6 (1.9)	11.8 (5.2)	15.0 (3.2)	10.3
D260	3.2	950	242.7	yes	57.7 (4.1)	11.4 (0.8)	13.7 (0.6)	11.6
D266	3.2	925	292.1	yes	56.0 (5.4)	10.9 (0.8)	14.7 (7.4)	10.0
14.5 wt. % H2O Experiments (H&Z +H2O)								
D200	3.2	1150	64.5	yes	57.7 (3.6)	0	15.0 (5.3)	0
D207	3.2	1125	52.5	yes	53.5 (0.9)	0	21.2 (1.4)	0
D205	3.2	1100	114.5	yes	54.3 (3.0)	2.5 (3.9)	21.8 (2.4)	5.3 (
D206	3.2	1060	48.2	yes	57.1 (4.9)	10.1 (1.6)	12.2 (8.9)	9.1 (
D165	3.2	1020	95.8	yes	56.8 (10.0)	10.2 (2.1)	17.9 (14.8)	11.5

Table 3. Analyses of selected experiments. Number below each oxide is one standard deviation of mean for glass and sample sta
phases. KdFeMg is for oliv/liq, oliv/opx, oliv/cpx and oliv/garnet, respectively.

	# of anals	SiO2	TiO2	Al2O3	Cr2O3	FeO	MnO	MgO	CaO	Na2O	K2O	NiO
D287												
oliv	13	40.8	0.02	0.01		8.47	0.08	50.2	0.06			0.09
		0.35	0.01	0.01		0.06	0.02	0.50	0.02			0.02
opx	18	56.63	0.04	2.29	0.61	5.32	0.10	33.97	0.90	0.03		
		0.30	0.02	0.18	0.16	0.12	0.01	0.22	0.04	0.03		
cpx	14	53.88	0.05	2.39	0.37	2.72	0.08	19.06	20.68	0.56		
		0.33	0.02	0.29	0.11	0.14	0.02	0.32	0.23	0.06		
garnet	13	42.18	0.14	21.52	2.72	6.88	0.24	19.61	7.25			
		0.32	0.04	0.47	0.68	0.11	0.02	0.39	0.47			
glass	309	47.71	0.74	13.03	0.28	8.21	0.14	16.10	11.33	1.96	0.44	
		0.19	0.02	0.07	0.01	0.06	0.00	0.26	0.31	0.05	0.02	
D284												
oliv	15	40.7	0.01	0.02		8.80	0.08	49.7	0.03			0.18
		0.29	0.01	0.01		0.11	0.02	0.60	0.02			0.08
opx	14	56.09	0.06	2.18	0.42	5.61	0.10	34.09	0.78	0.04		
		0.79	0.02	0.38	0.11	0.13	0.01	0.27	0.04	0.01		
cpx	15	54.29	0.07	1.98	0.57	2.51	0.07	18.19	21.17	0.50		
		0.36	0.01	0.11	0.09	0.10	0.01	0.24	0.23	0.03		
garnet	18	42.39	0.14	22.27	2.52	7.01	0.25	20.08	6.83			
		0.20	0.04	0.39	0.40	0.12	0.02	0.32	0.44			
glass	225	46.82	0.95	12.59	0.14	8.12	0.16	15.91	12.59	1.97	0.43	
		0.23	0.03	0.32	0.00	0.06	0.00	0.20	0.32	0.04	0.02	
D279												
oliv	13	40.41	0.02	0.02		9.09	0.078	49.59	0.06			0.16
		0.14	0.02	0.02		0.07	0.011	0.37	0.02			0.02
opx	15	56.54	0.07	2.02	0.45	5.85		33.83	0.71	0.04		0.05
		0.53	0.02	0.82	0.16	0.10		0.42	0.05	0.02		0.01
cpx	20	54.85	0.15	1.95	0.47	2.65		18.41	20.85	0.59		
		0.21	0.02	0.18	0.14	0.11		0.29	0.30	0.07		
garnet	21	41.72	0.22	22.83	1.66	8.09	0.28	19.34	6.25			
		0.18	0.06	0.52	0.60	0.10	0.02	0.47	0.52			
glass	350	48.72	1.34	13.48	0.12	7.38	0.12	14.44	9.14	3.95	1.26	
		0.20	0.02	0.06	0.00	0.05	0.00	0.16	0.21	0.04	0.03	
D276												
oliv	10	40.45	0.03	0.00		9.23	0.08	50.08	0.05			0.17
		0.23	0.01	0.01		0.08	0.01	0.45	0.02			0.05
opx	16	57.21	0.11	1.78	0.32	5.67	0.11	33.62	0.69	0.13		
		0.59	0.02	0.55	0.13	0.11	0.01	0.42	0.05	0.05		
cpx	18	54.12	0.18	1.92	0.56	2.64	0.06	18.03	21.50	0.70		
		0.50	0.05	0.20	0.13	0.17	0.01	0.87	0.63	0.08		
	# of anals	SiO2	TiO2	Al2O3	Cr2O3	FeO	MnO	MgO	CaO	Na2O	K2O	NiO
garnet	20	42.27	0.27	22.30	1.62	7.75	0.28	19.20	6.81	0.08		
		0.70	0.08	1.17	0.43	0.29	0.01	0.52	0.86	0.07		
glass	92	54.73	1.00	15.45	0.07	7.11	0.05	13.54	3.10	3.40	1.48	
		1.14	0.08	0.19	0.01	0.39	0.00	0.79	0.25	0.17	0.09	

spheres		55	73.93	0.06	16.86	0.03	0.54	0.02	1.01	0.95	4.39	2.15	
			0.22	0.01	0.12	0.01	0.06	0.00	0.10	0.08	0.20	0.06	
D255													
oliv		12	40.74	0.02	0.03		9.36	0.07	49.30	0.04			0.23
			0.19	0.01	0.02		0.11	0.03	0.48	0.02			0.07
opx		12	56.4	0.12	1.28	0.17	5.82	0.09	34.2	0.60	0.06		
			0.28	0.03	0.19	0.03	0.09	0.02	0.32	0.07	0.01		
cpx		11	54.0	0.26	2.03	0.38	2.63	0.08	17.6	20.9	0.84		
			0.23	0.04	0.38	0.07	0.12	0.01	0.41	0.30	0.14		
garnet		10	40.94	0.28	23.10	0.97	8.25	0.25	19.15	5.83	0.03		
			0.40	0.09	0.42	0.41	0.11	0.02	0.39	0.54	0.02		
glass		198	52.59	1.79	16.92	0.12	7.54	0.07	13.83	0.73	1.61	4.78	
			0.31	0.04	0.09	0.01	0.10	0.00	0.19	0.06	0.09	0.08	
spheres		24	72.77	0.17	17.34		0.61	0.01	1.24	0.29	4.24	3.15	
			0.57	0.05	0.32		0.14	0.00	0.28	0.06	0.28	0.13	
D250													
oliv		9	40.18	0.05	0.01		9.63	0.09	49.81	0.05			0.31
			0.12	0.01	0.01		0.10	0.01	0.37	0.02			0.04
opx		13	56.12	0.10	2.11	0.39	5.86	0.09	33.91	0.52	0.04		
			0.53	0.04	0.83	0.22	0.13	0.01	0.54	0.06	0.02		
cpx		13	53.89	0.26	2.42	0.72	2.52	0.07	17.14	21.41	0.97		
			0.38	0.03	0.53	0.16	0.15	0.02	0.23	0.51	0.12		
garnet		9	42.15	0.31	22.88	1.36	8.72	0.29	19.35	5.82			
			0.22	0.08	0.43	0.35	0.09	0.02	0.41	0.52			
glass		40	57.87	1.23	15.28		6.52	0.07	11.93	1.93	1.95	3.18	
			1.02	0.11	0.46		0.27	0.01	0.56	0.18	0.23	0.25	
spheres		7	76.57	0.49	11.15		2.67	0.03	2.40	1.43	1.87	3.36	
			1.17	0.12	0.99		1.50	0.01	0.51	0.49	0.73	0.54	
D252													
oliv		12	40.56	0.04	0.01		9.34	0.08	49.33	0.03			0.26
			0.42	0.02	0.01		0.17	0.02	0.46	0.02			0.06
opx		12	56.82	0.11	1.66	0.32	5.94	0.09	34.14	0.47	0.06		
			0.51	0.04	0.33	0.12	0.09	0.02	0.40	0.11	0.04		
cpx		10	54.73	0.29	2.50	0.81	2.48	0.06	16.96	21.14	1.28		
			0.37	0.03	0.21	0.08	0.09	0.01	0.32	0.23	0.13		
garnet		9	42.14	0.30	23.10	1.06	8.73	0.31	19.06	5.89			
			0.42	0.15	0.44	0.17	0.15	0.01	0.44	0.68			
glass		85	54.86	1.56	15.09		6.60	0.34	13.54	0.62	1.32	5.18	
			0.43	0.09	0.10		0.10	0.05	0.16	0.11	0.03	0.07	
D260	# of anals		SiO2	TiO2	Al2O3	Cr2O3	FeO	MnO	MgO	CaO	Na2O	K2O	NiO
oliv		7	40.39	0.02	0.03		9.27	0.06	49.07	0.09			0.33
			0.75	0.01	0.03		0.18	0.02	0.58	0.08			0.06
opx		17	56.83	0.10	1.59	0.30	5.97	0.09	34.02	0.38	0.11		
			0.56	0.02	0.40	0.13	0.09	0.01	0.32	0.04	0.03		
cpx		13	54.66	0.19	2.30	0.51	2.61	0.06	16.80	21.49	1.12		
			1.00	0.05	0.33	0.18	0.32	0.01	0.53	0.93	0.32		
garnet		15	41.63	0.25	23.69	0.34	9.45	0.29	18.73	5.44			
			0.29	0.11	0.30	0.14	0.11	0.02	0.47	0.55			
glass		58	58.27	1.57	15.15		5.25	0.04	10.43	1.10	2.70	5.31	
			0.85	0.38	0.25		0.33	0.01	0.60	0.17	0.19	0.18	

spheres		40	72.01	0.22	16.28		0.69	0.04	1.42	0.75	3.22	5.17	
			0.38	0.02	0.30		0.12	0.01	0.24	0.20	0.22	0.15	
rutile		5	0.21	96.17	0.54		1.04		0.26	0.06			
			0.46	0.58	0.11		0.06		0.08	0.02			
D266													
oliv		10	40.64	0.02	0.01		9.40	0.06	48.95	0.04			0.36
			0.32	0.02	0.02		0.12	0.02	0.58	0.03			0.07
opx		18	57.52	0.07	1.50	0.26	5.99	0.07	34.77	0.01	0.04		
			0.43	0.03	0.32	0.06	0.09	0.01	0.23	0.01	0.04		
cpx		22	54.57	0.15	1.21	0.31	2.38		17.76	23.00	0.36		
			0.38	0.03	0.41	0.08	0.19		0.41	0.60	0.09		
garnet		20	41.50	0.16	23.58	0.45	9.46	0.34	18.95	5.50			
			0.33	0.06	0.35	0.12	0.12	0.02	0.31	0.43			
glass	estimated		58.33	1.93	16.80	0.19	4.53	0.09	8.68	1.89	1.89	5.66	

Table 4. Analyses of glass in Till et al. (2012) experiments. Number below each oxide is one standard devi

	# of anals	SiO2	TiO2	Al2O3	Cr2O3	FeO
D200						
glass	299	49.38	0.61	16.37	0.20	7.37
		0.26	0.02	0.12	0.01	0.08
D207						
glass	516	48.71	0.67	13.84	0.16	7.95
		0.24	0.01	0.08	0.01	0.07
D205						
glass	46	49.91	1.50	17.18		5.71
		0.35	0.04	0.19		0.06
spheres	25	77.10	0.28	15.39		0.36
		0.39	0.05	0.40		0.07
D206						
glass	53	56.54	1.75	16.04	0.26	6.80
		0.85	0.28	0.38	0.06	0.21
D165						
glass	65	60.20	0.87	19.18		5.02
		1.50	0.13	0.91		0.62